UCLouvain

epl

École polytechnique de Louvain

Mechanical characterisation of polymer-based composites at fibre/matrix level by nano digital image correlation

Author: **Elise Van Vlierberghe**
Supervisors: **Thomas Pardoen, Yentl Swolfs**
Readers: **Bernard Nysten, Nathan Klavzer**
Academic year 2022–2023
Master [120] in Chemical and Materials Engineering

KU LEUVEN

FACULTEIT INGENIEURSWETENSCHAPPEN

Mechanical characterisation of polymer-based composites at fibre/matrix level by nano digital image correlation

Elise Van Vlierberghe

Thesis submitted for the degree of Master of Science in Materials Engineering

Thesis supervisors:
Prof. dr. ir. Thomas Pardoen
Prof. dr. ir. Yentl Swolfs

Assessor:
Prof. dr. ir. Bernard Nysten

Mentors:
Ir. Sarah Gayot
Ir. Nathan Klavzer

Academic year 2022 – 2023

Preface

Firstly, I would like to thank my supervisors, Professors Thomas Pardoen and Yentl Swolfs. I highly value the time they freed up for me, their patience and their immense knowledge. They kept on motivating me to seize every learning opportunity of this master's thesis.

I could not have undertaken this journey without my mentors, Sarah Gayot and Nathan Klavzer. I am extremely grateful for their guidance, their energy and their availability. I wish to show my appreciation to Sarah for her encouragement and help in the lab and to Nathan for his inspiration and thorough review of this text.

Special thanks to Sophie Vanpée for aiding with my subject definition, to Michaël Coulombier for the speckle deposition and to Laurence Ryelandt for the SEM training. I would like to extend these special thanks to Mahoor Mehdikhani for the help with the VIC-2D software and to Charline van Innis for showing me the RTM process.

Lastly, I would like to acknowledge my family and friends for their support and faith in me.

I dedicate this thesis to my dear grandmother, who passed away while I was working on it. Mamy, die altijd zo trots was op mij en me motiveerde om mijn passies na te streven, zelfs zonder haar.

Elise Van Vlierberghe

Contents

Abstract

Owing to a combination of low density and high stiffness and strength, fibre-reinforced polymers (FRP) are the material of choice for high-performance, lightweight applications. Given the heterogeneous nature of FRPs, multiscale bottom-up models are developed to predict the deformation and failure of composite components. Yet, to improve the numerical predictions and aid with the design of future composite structures, these models require constituent properties as input parameters. An accurate characterisation of the response of the constituents is thus essential. Existing multiscale models are currently lacking a complete understanding and reliable experimental data of the nano- and microscale stress and strain distributions. The literature points towards the presence of an in-situ effect on the matrix, meaning that its properties at the constituent level differ from those at the macroscale. Nanoscale digital image correlation (DIC) enables characterising the deformation and failure of the polymer matrix confined in between the fibres.

The goal of this master's thesis is to determine the nanoscale mechanical response in FRPs. For this purpose, glass/carbon fibre-reinforced amorphous thermoplastic/thermoset composites are examined by nano-DIC. Unidirectional samples were subjected to transverse compression within a scanning electron microscope. Nano-DIC relied on an indium speckle pattern of 15 nm in diameter to analyse several fibre configurations, classified according to a horizontal, vertical or diagonal position of two close fibres. Their corresponding nanoscale strain maps were characterised and compared while considering the thickness of the matrix strip separating the fibres and the macroscopic strain.

Nano-DIC allows identifying regions of strain concentration and shows that the strains tend to localise around the fibres. The formation of local submicron shear bands, oriented along the matrix strip, is captured in the resulting shear strain maps. The shear band orientation in vertical fibre configurations increased with the matrix strip length. The orientation obtained from nano-DIC coincided well with the literature. Furthermore, the failure locations in the regions of interest could be pre-emptively identified via concentrations of maximal shear strain values. A comparison of the local and macroscopic failure strains suggested a local increase in triaxiality.

The observed patterns are compared to finite element models based on constituent properties validated at the macroscale. The model results revealed similar patterns for the strain concentrations but showed inconsistencies in the local strain values and shear band orientations. Part of these discrepancies were related to the limitations of the model.

The results of this master's thesis consolidate the use of nano-DIC for the characterisation of FRPs at the fibre/matrix level, provide a systematic semi-quantitative framework to analyse and compare nano-DIC results across different systems and create valuable data for experimental validation of micromechanical models.

List of Figures and Tables

List of Figures

List of Tables

List of Abbreviations and Symbols

Abbreviations

AFM	atomic force microscopy
CF	carbon fibre
DIC	digital image correlation
e-beam	electron beam
FEA	finite element analysis
FRP	fibre-reinforced polymer
GF	glass fibre
In	indium
PMMA	polymethyl methacrylate
PVD	physical vapour deposition
ROI	region of interest
RTM	resin transfer moulding
RVE	representative volume element
SEM	scanning electron microscope
Sn	tin
TP	thermoplastic
TS	thermoset
UD	unidirectional
UTS	ultimate tensile strength

Symbols

A_0	initial cross-sectional area [m^2]
CV	coefficient of variation [%]
E	Young's modulus [Pa]
F	force [N]
K_{Ic}	fracture toughness [$Pa.m^{1/2}$]
L	length [m]
L_0	initial length [m]
M/F	matrix-fibre ratio [-]
T_g	glass transition temperature [K]
U	displacement [m]
V_f	fibre volume fraction [%]
γ_{max}	maximum shear strain [-]
γ_{xy}	shear strain [-]
ε_1	first principal strain [-]
ε_2	second principal strain [-]
ε_{eng}	engineering strain [-]
ε_{eq}	equivalent strain [-]
ε_{Lag}	Lagrangian strain [-]
ε_{log}	logarithmic strain [-] (strain representation in results and discussion)
ε_{macro}	macroscopic strain on specimen [-]
ε_{micro}	microscopic strain on RVE [-]
ε_{xx}	uniaxial strain in x-direction [-]
ε_{yy}	uniaxial strain in y-direction [-]
μ	mean
ν	Poisson's ration [-]
ρ	density [g/cm^3]
σ	standard deviation
σ_f	failure strength [Pa]
σ_{xx}	uniaxial stress in x-direction [Pa]

Chapter 1

Introduction

Owing to a combination of low density and high stiffness and strength, fibre-reinforced polymers (FRP) are the material of choice for high-performance, lightweight applications. FRPs are commonly known for their use in the aerospace industry, the development of sustainable mobility, and sporting goods. The entire application range of FRPs is displayed in Figure 1.1a and reveals that the automotive, construction and marine sectors account for about two-thirds of the FRPs market [1]. FRPs have been identified by several sectors as materials with a great weight reduction potential. Light-weight designs are an effective strategy to decrease greenhouse gas emissions [2]. For instance, the Boeing 787 Dreamliner is composed of 50 % of composite materials by weight (Figure 1.1b) [3] and the Airbus A350 XWB even of 52 %, which reduced the CO_2 emission by 25 % compared to similar-sized airplanes [4].

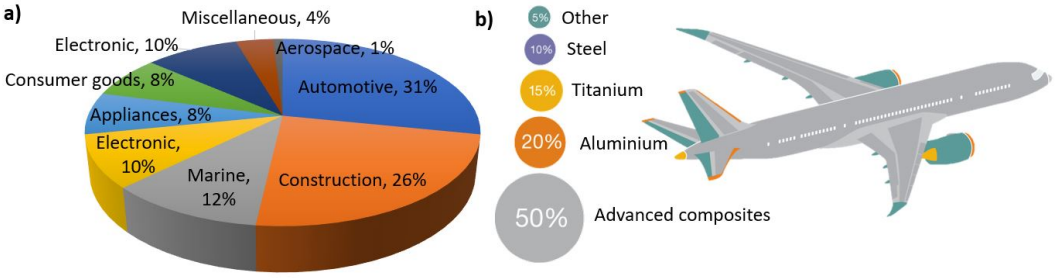

FIGURE 1.1: Applications of FRPs. (a) Market share of FRPs by application, adapted from [1]. (b) Material selection in the Boeing 787 Dreamliner airframe, adapted from [3].

Over the last few decades, due to demanding safety requirements for composite structures, such as in airplanes, the industry and the scientific community have been investigating FRPs. The mechanical properties of FRPs have been inspected from the microscale (i.e. individual constituents) up to macroscale (i.e. composite parts). The current goal is to predict the deformation and failure of composite structures by

simulations based on the experimental findings [5]. This would allow to improve the design of future composite structures and reduce the expensive quality tests on e.g. airframes ($\pm 10^4$ tests of material specimens) [6]. However, an accurate prediction of the failure stress of composite structure remains problematic due to the complex deformation mechanisms and failure scenarios of the hierarchical component [7, 8]. Multiscale modelling has been the preferred approach to perform virtual mechanical tests of composite structures [7, 9].

The scientific community is currently striving to provide physics-based microscale models to feed the multiscale models. Existing multiscale models are currently lacking a complete understanding and reliable experimental data of the nano- and microscale deformation and failure [9, 10]. The local mechanical behaviour of the matrix has been reported to differ from the bulk behaviour [9, 11–13]. More ductile behaviour on small specimens compared to large bulk specimens has been presented for epoxy resins [9, 14–17]. An interphase region between fibre and matrix has been indicated to range from a few nanometres to micrometres depending on the fibre sizing and the associated change of polymerisation conditions [9, 18, 19]. Many fundamental questions still remain regarding the local material response.

This master's thesis aims to mechanically characterise FRPs at the fibre/matrix level to improve the predictive capability of current computational models. Nanoscale digital image correlation (DIC) will be used to study the behaviour of the matrix in between fibres and attempt to understand microscale deformation processes. A finite element analysis (FEA), based on macroscale matrix properties, will be performed to differentiate the microscopic matrix response from that obtained from the simulation.

The materials of interest in this study are unidirectional (UD) composites of carbon-reinforced epoxy and glass-reinforced PMMA. Carbon and glass are two standard synthetic fibres. Carbon fibres (CF) have excellent mechanical properties for strengthening. They have however a low compressive strength and a high production cost. Glass fibres (GF) have high strength but somewhat lower modulus than CFs. The advantages of GFs compared to CFs are their isotropic properties and lower cost [1, 20, 21]. The matrix of an FRP consists typically of a thermoplastic (TP) or thermosetting (TS) polymeric material, which will be more extensively discussed in section "2.2.1 Glassy polymers" as it is the FRP constituent of interest in this study. In between the fibres and the matrix, the interface (and interphase) establishes the load transfer between these constituents. Chemical surface treatments of the fibres can improve their adhesion with the matrix and influence the interface properties [20]. The fibres and interphase are not the topic of this master's thesis but are closely related to the local matrix behaviour and will therefore be mentioned throughout this work for coherence.

Outline

The outline of this master's thesis follows the classical "introduction, literature review, materials and methods, results and discussion, and conclusion" format. Succeeding this first chapter with a general introduction, chapter 2 will detail the state of the art on the mechanical behaviour of glassy polymers and FRPs, as well as the previous research on DIC as a characterisation technique. Chapter 3 will elaborate on the experimental procedure of nano-DIC. The results of the nano-DIC are included in chapter 4 and compared to the FEA. Finally, chapter 5 will present the general conclusions.

Chapter 2

Literature review

The literature has been reviewed to set the scientific background of this master's thesis. Multiscale modelling of composites is first discussed as an application of nano-DIC, followed by a macro- and microscopic behaviour description of the composites of interest. Finally, nano-mechanical characterisation techniques are reviewed including an elaborate description of nano-DIC and the corresponding speckle pattern, DIC parameters and image distortions.

2.1 Multiscale modelling of composites

FRPs are excellent structural materials due to their combination of low density and high stiffness/strength. These exquisite mechanical properties result from the composite's hierarchical structure, shown in Figure 2.1. A composite structure consists of laminates that in turn are built of stacked plies with different fibre orientations. Each ply is made of a polymer matrix and fibres. Upon loading, several failure mechanisms occur simultaneously in these different elements (ply, laminate, component) and an accurate prediction of the failure stress of composite structures becomes a complex problem. Multiscale strategies aim to predict the failure of composites from the fibre/matrix scale up to the component scale and to enable virtual mechanical tests of composite structures. The bottom-up approach, presented by Llorca et al. [7], takes advantage of the hierarchical structure of composites and the separation of length scales. The properties of each element are computed at the relevant length scale using FEAs of representative volume elements (RVE). The resulting properties are homogenised into a constitutive model and passed on to the next length scale to determine the mechanical behaviour of this larger element. Multiscale modelling is thus realised by transferring information between different length scales [7, 8].

The first step in multiscale modelling uses computational micromechanics to predict ply properties (Figure 2.1). The FEA requires the properties of the constituents, i.e. fibre, matrix and interface, as input parameters [11]. Currently, micromechanical analyses typically include matrix models identified and validated at

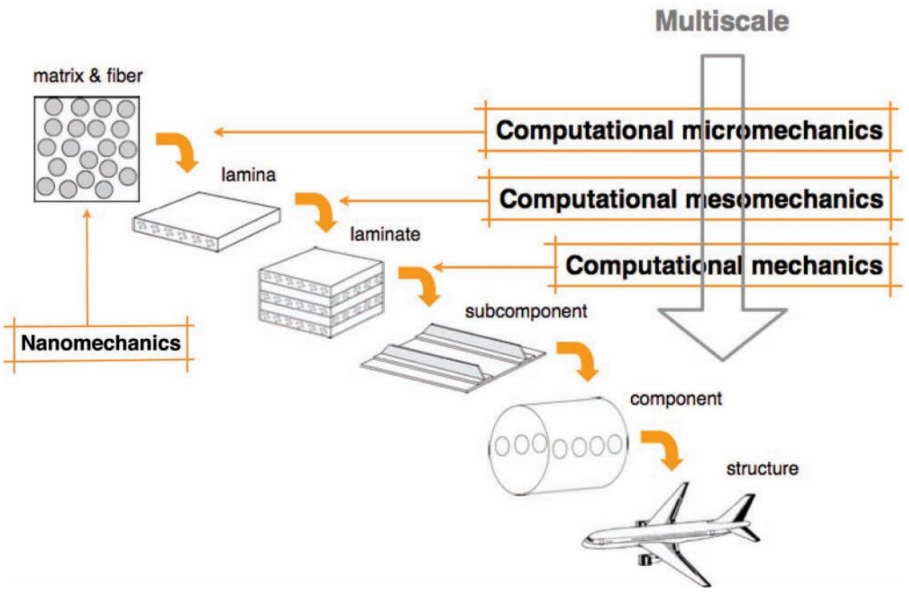

Figure 2.1: Multiscale modelling strategy to carry out virtual mechanical tests of composite materials and structures. Taken from [7].

the macroscale on pure polymer specimens. These macroscale matrix models do not take into account the impact of confined volumes on the matrix properties [22, 23] (section "2.3.1 In-situ effect on matrix"). Furthermore, the fibre/matrix interface input parameters are not entirely representative, as they often lack experimental validation [9]. Currently, the interfaces are almost exclusively represented by cohesive elements, which are defined by a strength parameter as the threshold for damage initiation in the element and an energy parameter related to its final failure [5]. The selected material parameters for the interfacial strength and toughness remain often very general [11], i.e. independent of the fibre/matrix system [22, 23]. Experimental results for the constituent properties are thus needed as input for the FEA, to improve the predictive capabilities of micromechanical models and of the virtual mechanical tests of composite structures.

2.2 Macroscopic mechanical properties of neat polymers

The polymer matrix in FRPs is the main carrier of the deformation in transverse compression, which is the loading mode examined in this thesis. The final failure of the composite by compressive stresses perpendicular to the fibres is accompanied by large deformations as a result of the non-linear response of the matrix [7, 24]. The mechanical behaviour of neat polymers is thus of interest as it affects the deformation of fibre-reinforced composites. In the following sections, the topology and mechanical behaviour of glassy polymers is detailed.

2.2.1 Glassy polymers

Polymers are organic materials of high molar mass and can be categorized according to their topology into thermoplastics, elastomers, and thermosets. TPs are reversible polymer networks physically bonded by entanglements. Depending on their state, TPs are classified as amorphous or (semi-)crystalline polymers, respectively with a random or crystalline lattice structure. At low temperatures, TPs are in a brittle, glassy state and are called glassy polymers. Amorphous TPs are in a viscous or rubbery state above their glass transition temperature T_g, whereas (semi-) crystalline TPs melt above their melting temperature. TSs are irreversible dense three-dimensional polymer networks chemically bonded by covalent cross-links. Below their T_g, TSs are also in a brittle, glassy state and are part of the glassy polymers. Above their T_g, however, the mechanical properties of TSs weaken [25].

Glassy polymers, both TP and TS, are commonly used as the matrix phase in FRPs and exhibit similar mechanical behaviour upon loading [26]. Meijer et al. [27] reported that the intermolecular interactions determine the elastic part of the mechanical properties, i.e. modulus and yield stress. The network controls the plastic part as it induces the necessary delocalization of local strain that gives toughness. The strain hardening modulus is directly related to the entanglement molecular weight. The mechanical behaviour of epoxy and polymethyl methacrylate (PMMA) are compared in Figure 2.2 as respectively a TS and an amorphous TP. According to the material index defined by Ashby [28], maximum flaw tolerance and strength can be obtained for displacement-controlled compression by maximising both the compressive strength σ_f and the ratio of the fracture toughness K_{Ic} and Young's modulus E. The material chart in Figure 2.2 displays similar mechanical behaviour for epoxy and PMMA compared to other polymers.

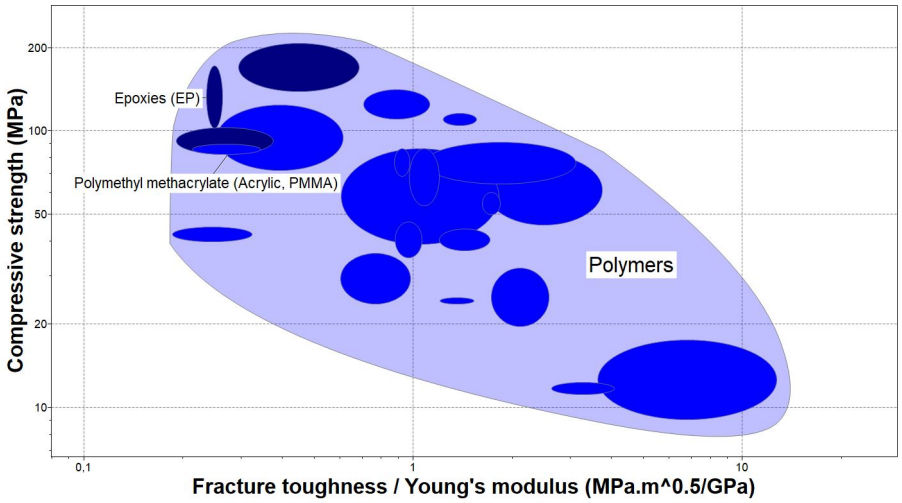

FIGURE 2.2: Material chart for polymers displaying flaw tolerance and strength during displacement-controlled compression.

Even though both glassy polymer types exhibit similar mechanical behaviour, TP matrices have recently gained renewed interest across many sectors where their TS counterparts are dominant. Obande et al. [29, 30] wrote that TPs are more desirable from an ecological point of view due to their recyclability, weldability and thermoformability. TSs do not soften remarkably at elevated temperatures like TPs as a result of their cross-linked network but offer more low-cost processibility than TPs. TPs have especially high-melt viscosities requiring high-cost processing techniques at elevated temperatures and pressures, rendering them impractical for most sectors. Currently, both glassy polymers thus appear to be a motivated choice for the matrix in FRPs.

2.2.2 Mechanical behaviour of glassy polymers

The mechanical behaviour of glassy polymers in compression follows the stress-strain curve displayed in Figure 2.3. Six characteristic stages of deformation are covered when increasing the compressive strain: an elastic-viscoelastic region, a yield transient, strain softening, strain hardening, unloading back-stresses, and strain recovery [5, 26].

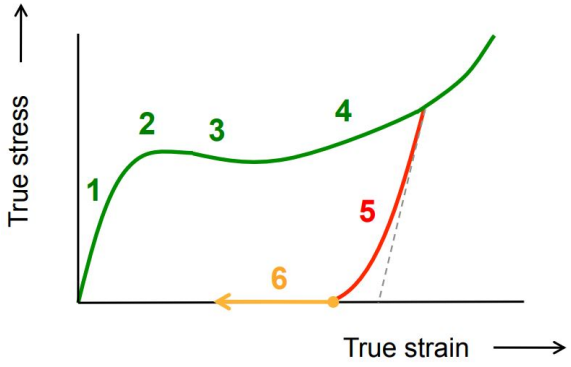

Figure 2.3: Schematic stress-strain behaviour of a glassy polymer in uniaxial compression: 1) elastic-viscoelastic region, 2) yield transient, 3) strain softening, 4) strain hardening, 5) unloading back-stress, and 6) strain recovery. Taken from [26].

The glassy polymer first enters the elastic-viscoelastic region, which is characterised by a reversible strain. G'sell et al. [31] distinguished these elastic and viscoelastic components from the plastic ones at higher strains. During the elastic deformation, the stress increases linearly with the strain with a slope of around 1-4 GPa defined as the Young's modulus E. The strains are resulting from inter-molecular resistance to molecular motion through van der Waals bonds [27, 32]. Still in the reversible regime, the viscoelastic region is entered when further increasing the stresses. A nonlinear decrease in the elastic slope is observed due to the limited delayed local molecular movements allowing stress relaxation [33].

The glassy polymer then transitions from the elastic to the plastic regime in the yield transient. This region is marked by the yield point, which was defined by Rabinowitz et al. [34] as the local maximum of the stress-strain curve. The stresses are now high enough to overcome the activation barrier for chain mobility as the stress-induced chain rotations conquered the intermolecular forces. The moving chains induce an irreversible change in configuration and the strain can no longer be directly recovered [27, 32, 35].

When the stress decreases after the yield point, the glassy polymer has entered the strain-softening region. Bowden et al. [35] differed extrinsic softening, which is triggered by the geometrical features of the test from intrinsic softening. The extrinsic plastic deformation is localised in shear bands, which are narrow X-shaped zones of intense shear strain (Figure 2.4). The shear bands were initiated before the yield point and are now thickening. Macroscopic shear bands represent large diffuse zones of about 1 mm, consisting of multiple microscopic shear bands depicted as highly localised fine bands of about 1 µm [35]. The physical origin of intrinsic softening is not entirely understood and a debate is ongoing between strain rate effects [35, 36] and the distribution of activation energies [37, 38].

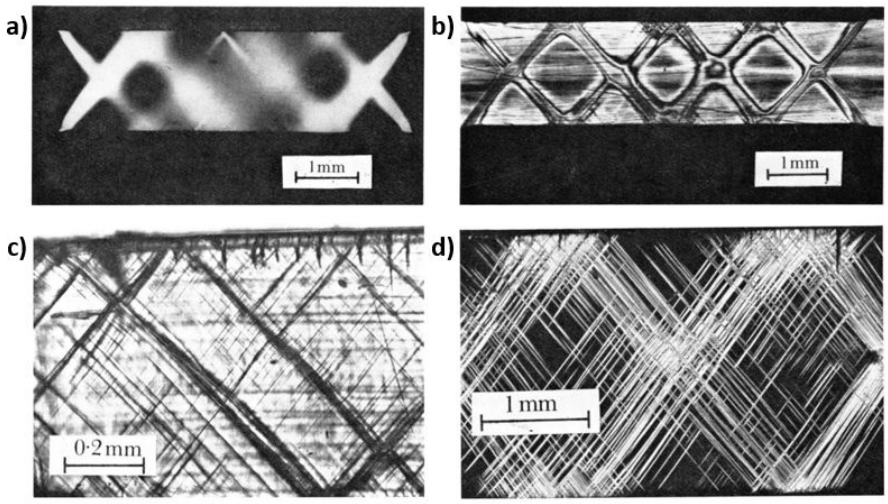

FIGURE 2.4: Shear band patterns in various glassy polymers, deformed under plane strain compression at 22 °C and viewed between crossed polarisers: a) polymethyl methacrylate (PMMA), b) polyvinyl chloride (PVC), c) polyethylene terephthalate (PET) and d) polystyrene (PS). Adapted from [35].

After that, the stresses increase again at larger strains and the glassy polymer is then in the strain-hardening region. G'sell et al. [39] related this behaviour to the gradual alignment of the macromolecules. The stress-strain curve is then dictated by the response of the entangled or cross-linked network [40]. Hoy et al. [41] reported also viscous contributions to strain hardening besides its entropic nature [40]. The

ratio of strain softening and hardening determines the failure process in glassy polymers, which will be discussed in section "2.3.2 Fracture mechanisms". Pronounced strain softening leads to extreme strain localisation and crazing, whereas pronounced strain hardening leads to stable localisation and necking [27, 42].

When the compression is withdrawn, unloading back-stresses appear in the glassy polymer. This nonlinear Bauschinger effect is thought to be the translation of a facilitated reversed deformation due to internally built-up back-stresses [35, 40] but not entirely understood at the moment [26].

Finally, the glassy polymer enters the strain recovery regime after unloading, including relatively large strain recovery of apparent plastic deformation [32, 35]. This characteristic has not often been discussed in the literature [26]. Overall, the literature widely covers the observation of features related to the stress-strain behaviour of glassy polymers but not all origins of such behaviour have yet been unveiled.

2.3 Micromechanics of fibre-reinforced composites

The macroscopic deformation and failure of FRPs are dictated by phenomena at the microscale, which is the size of the relevant microstructural features like the fibre diameter [43]. The initiation and propagation of the local micromechanisms depend on the loading direction relative to the fibre direction (Figure 2.5), the constituent material properties, and the local fibre distribution. During longitudinal loading, the fibres are carrying the deformation. Longitudinal tensile failure is dominated by fibre strength and longitudinal compressive failure by fibre buckling. During transverse and shear loading, the matrix and interface control the deformation. Transverse tensile failure favours progressive damage accumulation at the interface and matrix cracking. Transverse compressive failure favours matrix plasticity, e.g. shear bands. Both transverse failure modes are accompanied by fibre/matrix debonding [11, 44]. The following sections will specify the in-situ effect on the matrix and the fracture mechanisms at this microscale.

2.3.1 In-situ effect on matrix

At the constituent level, the properties of the matrix differ from those at the macroscale. The polymer matrix is affected by the presence of the fibres and is constrained in interconnected microscale regions of 1-25 µm, up to even 200 µm in between reinforcement layers [17]. The mechanical properties of the polymer matrix also vary when reaching the fibre, creating an interphase [45].

Hobbiebrunken et al. [14] introduced hot drawing as a production method for epoxy resin microfibres with an average diameter of 27 µm, similar to the confined volume inside a composite. They measured an increase in ultimate tensile strength (UTS) as the gauge volume decreased. They obtained an epoxy fibre UTS that was

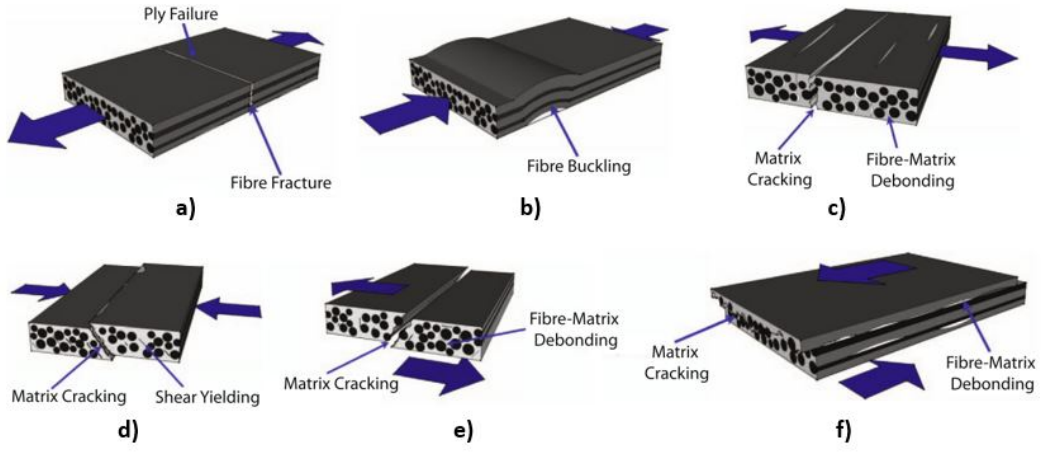

FIGURE 2.5: Fibre-reinforced microscopic failure mechanisms under (a) longitudinal tensile loading, (b) longitudinal compressive loading, (c) transverse tensile loading, (d) transverse compressive loading, (e) transverse shear loading and (f) longitudinal shear loading. Taken from [44].

180 % of that of the bulk specimens and approached the theoretical UTS of the polymer. Misumi et al. [15] extended this research and confirmed the increase in UTS in the microfibres for five different epoxy systems. They also noticed an increase in failure strain (1.7-4.9 % macroscopic vs. 20-42 % microscopic) and a similar stiffness (±3 GPa) compared to the bulk specimens. Sui et al. [16] expanded the microfibre research over a broader range of diameters and studied mechanical properties under tension. They showed that a decrease in diameter results in an increase in UTS (strength $\sim 1/(\text{fibre diameter})^{\beta}$ and $\beta \geq 2$) and ultimate strain as well as an increase in toughness. They, however, reported an increase in stiffness contrary to Misumi et al. [15] but according to Verschatse et al. [17] this could be related to experimental deviations (such as differences in conversion and different testing methods). Verschatse et al. [17] continued the research on epoxy microfibres with varying diameters. They observed for the microscale specimen a large plastic deformation via the formation of a necked zone that extended throughout the fibre, whereas the bulk epoxy showed brittle behaviour (failure strains up to 130 % for microfibres vs. 8 % for bulk).

The mechanical behaviour of the matrix clearly shows a size dependency but there is currently no agreement on the origin of this in-situ effect. Pardoen et al. [9] raised questions on local curing conditions in between the fibres possibly influencing the matrix properties, or mechanical confinement perhaps affecting the development of plasticity. Verschatse et al. [17] mentioned the possibility of a size effect related to the size of defects inside the material. The small size of the confined matrix region limits the size of voids which delays tensile failure and enables higher plasticity. Another possibility, according to them, is the difference in microstructure

due to for example the orientation of polymer chains. They have shown that the orientation of polymer chains in the microfibres is negligible prior to testing but confirmed the molecular reorientation in necked epoxy fibres that Sui et al. [16] had revealed. Verschatse et al. [17] linked the high plastic deformation in microfibers to the rearrangement of the polymer chains during necking as a result of chain slippage and some orientation along the tensile loading direction. Further, they brought up that the production method could induce the in-situ effect, for example by a difference in conversion degree, like Pardoen et al. [9]. Finally, Gregory et al. [12] suggested that a complex interaction of the molten matrix phase with fibre coupling agents likely also contributes to the variation in mechanical properties. Regardless of the cause, the mechanical properties of the matrix in confined volumes differ from the bulk properties. It does need to be accounted for to enable a reliable multiscale modelling approach (section 2.1).

2.3.2 Fracture mechanisms

TP and TS matrices present dissimilar damage evolution behaviour linked to their topology (section 2.2.1). Both polymers show distinct fracture mechanisms with TPs being rather ductile and TSs rather brittle [29]. Van Melick et al. [42] linked ductile failure with pronounced strain softening and brittle failure with pronounced strain hardening. Ductile behaviour is characterised by largely spread localised plastic zones, which leads to higher stress and strain at failure. These plastic zones progress from shear bands to necking. Brittle behaviour shows more extremely localised plastic zones, which lead to micro-cavitation, crazing and sudden failure at relatively small deformation.

Chevalier [5] summarised that, in glassy polymers, the density of entanglements for TP or the degree of crosslinking for TS characterises the mobility of the polymer chains and thus crazing. The formation of micro-voids and small fibrils to develop crazes is hindered by the entanglements or crosslinks. Crazing is the main damage mechanism under positive stress triaxialities, leading to brittle fracture. When crazing is prevented by the entanglements or crosslinks, or by loading conditions (e.g. in compression), shear bands develop in the matrix.

Shear bands are a result of strain softening of the polymer matrix as was introduced in section 2.2.2. González et al. [46] demonstrated that shear bands orient along 52.5° with respect to the loading direction under transverse compression. Hu et al. [22] then demonstrated that the shear band orientation depends on the fibre volume fraction V_f, as it ranges from 52.5° for a pure matrix to 60.0° for FRPs with a high V_f. It should be noted that for shear banding to cause failure, the interface shear strength should be larger than the matrix yield strength. For low interface strength, fibre/matrix debonding would lead to early failure [5, 46]. As reminded by Hardiman et al. [44], the large number of microscopic failure mechanisms complicates failure predictions and quantitative experimental confirmation of the micromechanical models is still lacking.

2.4 Nano-mechanical characterisation

To feed the multiscale FEA, the properties of the constituents are needed. As mentioned in section 2.3.1, confining the matrix in small volumes in between the fibre affects the mechanical properties. Therefore, it is crucial to develop methods that allow for accurate measurements at this scale. Nano-mechanical characterisation techniques focus on the fibre/matrix level and can unravel the fundamental mechanisms of deformation and failure at this scale. Digital image correlation, nanoindentation, atomic force microscopy, and fibre pushout are presented in the following sections. Digital image correlation, the method used in this thesis, is further detailed and information on the speckle pattern, the parameters and image distortions are given.

2.4.1 Digital Image Correlation

DIC is an optical, noncontact technique used to analyse the mechanical properties of various material systems. It allows measuring full-field 2D displacements over the surface of a deforming material and calculating its corresponding strain fields. The general principle is to record a series of digital images and to track the relative displacement of discrete material points between a reference (undeformed) image and a current (deformed) image. These material points can be surface features inherent to the material (e.g. fibres in composites) or an artificial random speckle pattern from the deposition of small particles. The displacement correlation process, shown in Figure 2.6, virtually divides the pattern into unique subsets and uses their grey intensity levels to extract positional information [9]. DIC is a widely-used method and gained in popularity due to the general (apparent) simplicity of the sample preparation and optical setup, and the availability of commercial packages. Any length scale can be studied, from metres to nanometres, as long as a pattern can be properly generated and imaged [47].

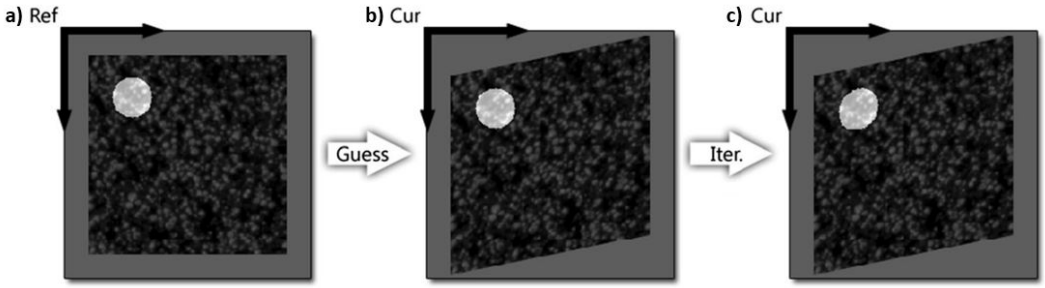

FIGURE 2.6: Schematic of the DIC algorithm (a) reference image with one round subset (b) initial guess for the displacements (c) iterative solution for strains. Taken from [48].

At the microscopic scale, DIC can be used to indicate the influence of the microstructure on the deformation processes. Measurements of full-field displacements with a spatial resolution of about 1 µm, are obtained using a scanning electron microscope (SEM), as a result of its large depth of field and high resolution of 1-4 nm [49]. µDIC has been mostly applied to metals until Canal et al. [43] demonstrated the potential of µDIC in the study of FRPs. They performed in-situ transverse compression tests inside an SEM to record sequences of deformation and fracture events in a UD E-glass/epoxy composite. Long-range fluctuations in strain due to the presence of matrix-rich and fibre-rich zones were captured within the region of interest (ROI) and its average composite strain was accurately determined. The average strain in the individual phases could not be correctly quantified, as the µDIC analysis was respectively under- and overestimating the strains in the matrix and the fibres. This was the result of the smoothening of the sharp strain gradients at the fibre/matrix interface in the correlation process.

Mehdikhani et al. [50] continued this trend of µDIC in the study of FRPs and demonstrated the importance of evaluating the errors related to µDIC. UD GF-reinforced composites were loaded in transverse three-point bending inside an environmental SEM and their tensile deformation was imaged. A good agreement between the µDIC measurements and FEA maps was achieved and regions subjected to strain concentrations were identified. Still, the problem of the smoothening of the sharp strain gradients at the fibre/matrix interface withheld the detection of small-scale strain concentrations as well as strains at the interface. In a following study, Mehdikhani et al. [51] investigated µDIC for measurements of strain fields in hierarchical FRPs, here an alumina fibre/epoxy composite laminate with aligned carbon nanotubes grown on fibres. Utilising an environmental SEM and a high-quality random nanoscale speckle pattern ($\varnothing = \pm 220$ nm), the influence of the aligned carbon nanotubes on the deformation field around the fibres was detected.

However, studies on µDIC for FRPs remain rare because of the numerous challenges related to this technique. Practical challenges include equipment limitations (in-situ testing in an SEM), stress relaxation during image acquisition and tedious small-scale specimen preparation (machining, polishing, speckle pattern deposition). The accuracy of µDIC is limited due to errors resulting from the speckle pattern quality, DIC analysis parameters and SEM artefacts (e.g. charging, spatial and drift distortion, noise) [50].

Recently, Klavzer et al. [10] developed a nanoscale DIC technique for FRPs, overcoming the smoothening of the sharp strain gradients at the fibre/matrix interface. Their work did not yet include the interpretation of the nano-DIC data and that will be the topic of this master's thesis.

Speckle pattern

A proper DIC analysis yielding quantitative information requires a high-quality speckle pattern for the displacement correlation. Medhikani et al. [50] reported that areas free of speckles lead to more significant errors and influence the accuracy of the DIC results. The speckle pattern must conform to the length scale of interest and provide enough grey-level contrast at this scale for the DIC algorithm. Since the accuracy and the resolution of the measurements depend on the nature of the speckle pattern, a random deposition of small speckles seems to be a suitable option. This homogeneous and dense pattern would be independent of the material and fine enough to measure local displacements, as suggested by Canal et al. [43]. Further, Hoefnagels et al. [52] recommended that an optimal pattern for DIC should be able to sustain highly localised strains without showing pattern degradation or changes. It should also be applied without altering the nature of the specimen and accordingly avoiding heat treatments, pressure, or chemical reactions.

The terminology of "nano-DIC" used in this thesis is based on the technique's resolution of a few tens of nanometres and for this, a nanoscale patterning technique is needed. Two types are currently employed: the dispersion of nanoparticles and the deposition of a metal. The first method, achieved by drop casting or mystification of droplets of nanoparticles in a solvent, is however sensitive to clustering and not easily reproduced. The second method consists of first depositing one or more metal (e.g. gold or silver) layers of homogeneous thickness followed by a heat treatment to provoke the reconstruction of this layer into separate islands [52].

Hoefnagels et al. [52] developed a patterning method based on the deposition of metal without subsequent heat treatment. They propose a one-step deposition of low-melting temperature solder alloy islands using physical vapour deposition (PVD) by magnetron sputtering. The speckle pattern is formed by Volmer-Weber growth, also known as island growth. This mechanism grows a thin film by nucleation, growth, and coalescence of separate islands. This requires a large surface diffusion length of the metal adatoms which typically only occurs at a very high substrate temperature, which in turn could affect the specimen properties. Direct island growth, without specimen heating, may still be achieved by depositing metal adatoms with a high surface mobility (e.g. low-melting temperature alloys) while supplying high kinetic energy to boost the adatoms. This was proven for (near-) room temperature deposition of InSn patterns by PVD on metallic substrates. They successfully quantified strain localisation in polycrystalline iron foils over large areas with feature sizes ranging from approximately 10 nm to 2 µm.

The processing method of Hoefnagels et al. [52] provides sufficient freedom to control morphologies, like particle shape, size, and density. Considering that the deposition time influences the speckle pattern morphology (Figure 2.7), the size of the islands can be tuned for any DIC scale. Klavzer et al. [10] adapted the deposition technique for the application of nano-DIC on FRPs. They deposited indium (In) by electron beam (e-beam) evaporation onto polymer composite substrates.

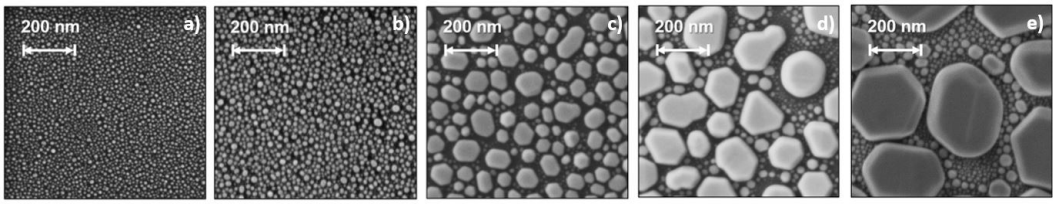

Figure 2.7: Influence of deposition time on speckle pattern morphology: SEM micrographs of a (a) 2 nm, (b) 5 nm, (c) 10 nm, (d) 20 nm, and (e) 50 nm-thick indium target coating deposited by e-beam evaporation onto Si wafers. Taken from [10].

DIC parameters

The strain resolution of the DIC analysis depends on the DIC parameters such as subset and step size seen in Figure 2.8. Carter et al [53] reported a trade-off to define the optimal set of parameters. Increasing the strain resolution corresponds to decreasing the noise, which has both intensity and spatial components. Amplifying the intensity resolution simultaneously lowers the spatial resolution. Measuring strain localisation by DIC requires high spatial resolution more than the absolute intensity value and this weighs in on the trade-off.

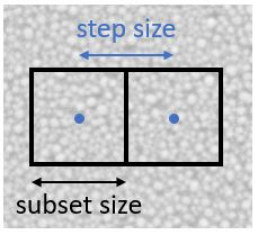

Figure 2.8: Schematic of DIC parameters including subset and step size.

The DIC algorithm divides the image into subsets to correlate the motion of the speckles. Increasing the subset size reduces the intensity noise distribution because larger subsets hold more speckles and can thus be detected more accurately. Increasing the subset size, however, reduces the spatial resolution at the same time, as local variation may not be captured precisely. The optimal subset size should compromise between a small value for details and a large value for an accurate result [50]. Bornert et al. [47] documented that the subset size is the ultimate spatial resolution and its minimum value depends on the speckle density. This is the reason that the DIC algorithm is incapable of correlating the images when the subset size is of the same size as the spacing between the speckles.

The spacing of the points analysed in DIC is defined by the step size. Decreasing the step size reduces the spatial noise because smaller step sizes analyse more pixels and can thus yield more detailed correlations. However, reducing the step size also

increases the intensity of noise, similar to the subset size [50]. Carter et al. [53] have shown that increasing the subset size produces less spatial noise than increasing the step size. Therefore, the best spatial resolution to capture strain localisation is obtained with a moderate subset size and a small step size.

The DIC algorithm also includes a smoothing filter to apply to the strain calculation after the correlation. The smoothing filter, or strain radius, reduces the noise on the resulting strain. Analogous to the other DIC parameters, the spatial resolution is increased by using a smaller filter but it implies more noise on the intensity distribution of the strain [50].

Image distortions

Acquiring DIC data with an SEM generates considerable potential for image instabilities that could cause errors in µDIC, especially at high magnification. These deviations from the 'ideal' image position are so-called image distortions and include space- and time-dependent effects, respectively called spatial and drift distortion. Sutton et al. [54, 55] have demonstrated that image errors are a generic feature of the SEM imaging system by observing that image shifts occur at random positions during the scanning. These positional errors occur due to a variety of system and environmental variations and decrease the accuracy of the DIC measurements.

Spatial distortions remain relatively constant throughout an experiment and depend only on the pixel position in the image. They arise, among other things, due to electromagnetic lens aberrations and are more prevalent at low magnification. In micro and nano-DIC, spatial distortion is thus a limited problem. The space-dependent effects can be quantified, without modifying the DIC algorithm, from translated image pairs captured before deforming the specimen, as described by Kammers et al. [56]. Since the imposed displacement between the translated image pairs is known, it is subtracted from the displacement field obtained by DIC to yield spatial distortion maps. The linear relationship between the amplitude of the distortion and the imposed translation can be used as a correction function.

Drift distortions arise mostly from the charging of the specimen but also from the charging of the SEM equipment, motions of the SEM stage, heating of the equipment and the specimen, and disturbance from magnetic fields [51]. Kammers et al. [56] demonstrated that drift distortions are more significant at high magnifications, contrary to spatial distortions, and can thus generate erroneous micro and nano-DIC results. The time-dependent effects can be quantified, without modifying the DIC algorithm, from consecutive image pairs captured during the experiment. Drift distortion maps are yielded by subtracting the obtained displacement maps from one another. The horizontal and vertical displacement maps serve as a correction tool as they can then be subtracted from the current DIC displacement maps to obtain drift-free maps [10].

Klavzer et al. [10] have applied these distortion corrections to nano-DIC on FRPs (Figure 2.9). They obtained relatively low spatial and drift corrections, which they related to proper sample preparation and excellent grounding. Neglecting corrections on their nano-DIC measurements induced at most a displacement error of around 0.5 µm for an applied displacement of 4 µm.

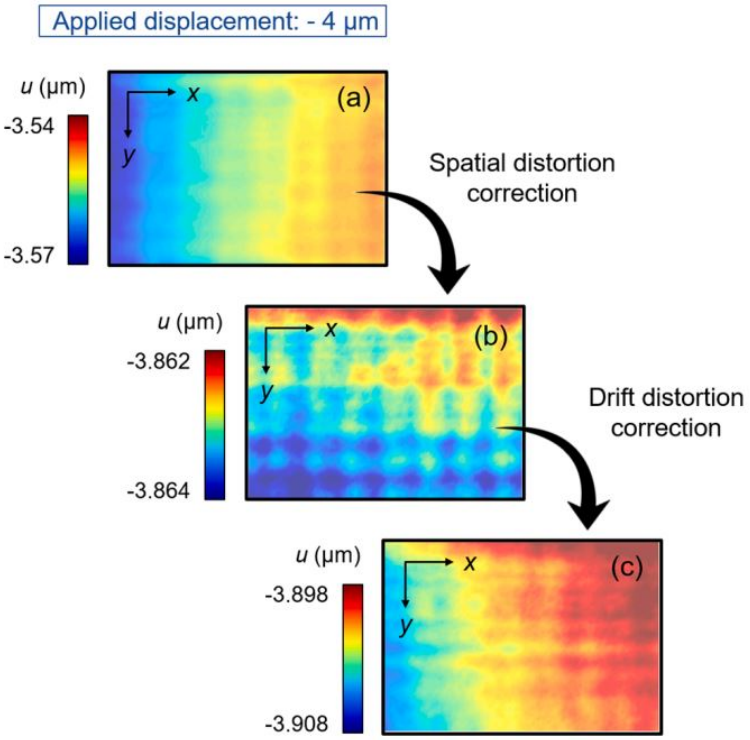

Figure 2.9: Horizontal displacement field measured by DIC: (a) without any correction, (b) after spatial correction and (c) after spatial and drift corrections. Taken from [10].

Other image instabilities include random noise and stress relaxation. Random noise is strongly dependent on SEM imaging and could be reduced by optimising the imaging parameters [51]. Long image scans lower the random noise but can capture stress relaxation in the sample. Stress relaxation is strong in polymer glasses and it generates gradients on the DIC displacement maps. Kammers et al. [56] emphasized the importance of stress relaxation correction. They reported that performing drift corrections without correcting for stress relaxation can result in larger errors than for uncorrected data. They related stress relaxation-induced displacements to the load drop during image capture. This relation was applied to adapt the distortion correction framework of Sutton et al. [54, 55] to account for stress relaxation.

2.4.2 Other techniques: nanoindentation, atomic force microscopy and fibre pushout

In-situ nano-DIC compression tests evaluate nanoscale deformation and failure mechanisms. When combined with other methods an improved characterisation of the behaviour at the elementary fibre/matrix level can be obtained, including micro- and nanoscale properties on the elastic, plastic, creep and fracture features. Nanoindentation, atomic force microscopy (AFM) and fibre pushout, shown in Figure 2.10, enable the characterisation of local properties of the constituents of FRPs. These properties permit feeding the simulations of in-situ compression tests and quantitatively validating the nano-DIC results. However, some controversies remain around the data analysis of these techniques [9], as will be mentioned in the following paragraphs. Nanoindentation and AFM focus on matrix characterisation like nano-DIC in this work. Fibre pushout and AFM on the interphase, which is closely related to the local matrix behaviour.

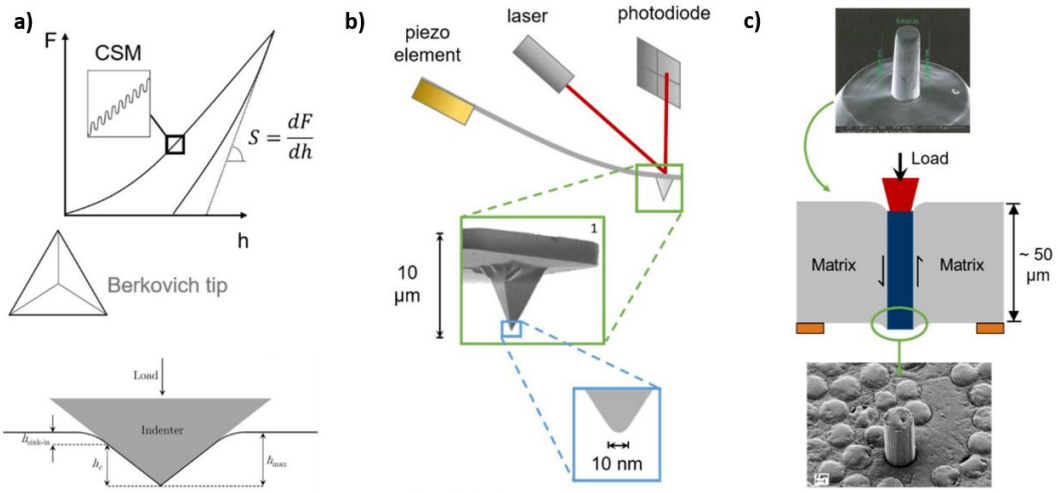

FIGURE 2.10: Principle of several nano-mechanical characterisation techniques. (a) Nanoindentation: typical obtained load-displacement curve with small oscillating load for CSM highlighted, Berkovich indenter tip and schematic representation of nanoindentation test. (b) AFM: instrumentation and length scales. (c) Fibre pushout: micrograph of a typical nanoindenter flat tip, schematic representation of the single fibre pushout test and micrograph of a debonded fibre at the end of a test. Adapted from [9].

Nanoindentation (Figure 2.10a) is a non-destructive technique to obtain the hardness and elastic indentation modulus at the nanoscale. A three-sided pyramid-shaped Berkovich tip is pressed into the sample under load and subsequently unloaded. For each indent, a load-displacement curve is acquired and subjected to Oliver and Pharr's method [57] to extract stiffness and hardness. Besides this classic depth-sensing indentation method, a continuous stiffness measurement mode

accounts for indentation size effects. An oscillating force is superimposed on the main loading to obtain a continuous measurement of the contact stiffness as a function of the indentation depth [44]. Nanoindentation is widely used to determine constituent properties of composite materials including polymer matrix in near-fibre confined volumes. Up to 20 % higher hardness and modulus values were obtained for the polymer matrix in FRPs compared to the pure polymer [11–13, 44]. However, the classic protocols remain controversial as the size effect at low indentation depths calls for more advanced constitutive model developments, able to incorporate the constrained mobility of the polymer chains under the indenter [9].

AFM (Figure 2.10b) is a surface analysis technique used to obtain elastic modulus and surface topography at the nanoscale. A microscopic tip attached to a flexible micro-cantilever interacts with the surface, causing the tip to move. A laser bounces off the back of the cantilever and changes direction with the deflection of the cantilever. A photodiode captures the change in position of the laser beam on the detector and relates this displacement to the vertical displacement of the cantilever. In contact mode, the deflection of the cantilever is kept constant and its vertical displacement is measured. In tapping mode, the cantilever is not in constant contact with the sample surface but oscillates at its resonance frequency to avoid damage. This mode ensures a constant tip-surface interaction force by modifying and measuring the oscillation parameters of the cantilever [18]. AFM is widely used in the field of composite materials for the mechanical characterisation of the local behaviour of the matrix and the interphase region around the fibres. Bahrami et al. [58] related matrix modulus variations to the degree of curing by measuring more compliant, incompletely cured domains at the nanoscale. Also, an interphase region with sharp changes in mechanical properties was measured to range from a few nanometres to micrometres depending on the fibre sizing and the associated change of polymerisation conditions [9, 18, 19]. Yet, the quantification of the constituent properties remains limited due to the interaction volume of the tip sensing the fibre. The limitations are similar to those for nanoindentation but much more localised for AFM [9].

Fibre pushout (Figure 2.10c) is a fibre indentation test to obtain interface properties of the composite at the constituent level. A single fibre in a thin composite slice is loaded using the tip of a nanoindenter. The compressive load is increased until the fibre is entirely pushed out of the specimen. Debonding between fibre and matrix then occurred due to the arising shear stress [59]. Fibre pushout has been used in a few studies on FRPs, aiming to understand the mechanical behaviour of the interfacial region and delay the onset of decohesion. However, FEA is always needed to extract the interface properties and, as mentioned in section 2.1, modelling the microscale behaviour of composite materials still faces challenges [9]. Hence, this aspect still requires more attention in the scientific community.

2.5 Conclusion and premise for current work

Multiscale modelling was proposed as a simulation technique to predict the failure of composites from the fibre/matrix scale up to the component scale. These models require the constituent properties as input parameters and an accurate characterisation of the response of these constituents is thus essential. Macroscopic mechanical properties of neat polymers were revised with a special interest in glassy polymers. Currently, matrix models identified and validated at this macroscale on pure polymer specimens are typically included in micromechanical analyses. Micromechanics of fibre-reinforced composites were recapitulated, noting that during transverse and shear loading, the matrix and interface control the deformation. The in-situ effect on the matrix was examined, since, at the constituent level, the properties of the matrix differ from those at the macroscale. Several nanoscale characterisation techniques were studied to assess the mechanical properties at the fibre/matrix level, including nano-DIC.

Based on the latest advances in surface patterning, Klavzer et al. [10] developed nano-DIC for FRPs. The dense, homogeneous indium speckle pattern with a particle diameter of about 15 nm allowed overcoming the smoothening of the strain gradients at the fibre/matrix interface by µDIC. The displacement correlation process could now differentiate two phases, as the window in which the derivative of the displacements is taken to calculate the strains is small enough to capture the fibre/matrix interface. They subjected a CF-reinforced TS and GF-reinforced TP to transverse compression in an SEM and optimised the settings such as the speckle pattern, the DIC parameters and image distortion corrections. This novel nano-DIC method captured strain concentration areas as submicron shear bands and fibre/matrix interphases for both composites. This master's thesis is a continuation of their work to use nano-DIC to unravel the fundamental mechanisms of deformation and failure at the fibre/matrix level.

Chapter 3

Materials and methods

This master's thesis aims to mechanically characterise FRP composites at the fibre/matrix level by nanoscale DIC. Hence, UD composite samples were manufactured and coated with a speckle pattern for in-situ transverse compression testing. Three fibre configurations were chosen to analyse with two DIC software packages, Ncorr and VIC-2D. The calculated strain fields were then displayed to reveal strain localisation phenomena. An FEA was performed for validation of the observed strain localisation patterns respective to the fibre configuration. A graphical representation of the experimental procedure is included in appendix A.1.

3.1 Preparation of unidirectional fibre-reinforced polymer composite samples

UD samples were manufactured for the in-situ transverse compression tests. Two composites were analysed: a GF-reinforced amorphous TP and a CF-reinforced TS. Cuboid samples were machined out of the obtained composite plates and were then polished to a mirror finish.

3.1.1 Glass fibre-reinforced PolyMethyl MethAcrylate composite

The UD GF-reinforced amorphous TP composite samples were provided by Arkema (France). They manufactured continuous UD composite profiles, with a final thickness of 2 mm and a V_f close to 65 %, by pultrusion. The TP matrix consisted of Elium® 591 (Arkema), which is a pultrusion-grade methyl methacrylate-based monomer formula, with the addition of 1/100 peroxide thermal initiators, Perkadox® 16 (Nouryon, the Netherlands), Trigonox® 141 (Nouryon) and Luperox® DEC (Arkema). The reinforcements were 2400-tex SE 4740 glass rovings (3B-The Fiberglass Company, Belgium) [10].

3.1.2 Carbon fibre-reinforced epoxy composite

The UD CF-reinforced TS composite samples were provided by UCLouvain (Belgium). They were produced by resin transfer moulding (RTM) according to the method described by Chevalier et al. [11], which yields slabs with V_f close to 40 %. The TS matrix consisted of the monocomponent HexFlow RTM6 resin from Hexcel (Connecticut, USA). The reinforcements were HTS 12K CFs (Saertex Gmbh, Germany) [10].

3.1.3 Sample geometry

For both composites, cuboid samples were machined out of the obtained composite plate using a water-cooled disc milling cutter (Accutom-5, 0.005 mm/s, Struers Inc., Ohio, USA). The geometry was chosen to fit with the compression stage. Firstly, it should enable failure below 2 kN, corresponding to the load limit of the compression stage. Secondly, the height of the sample (along fibre orientation) was set to 3 mm, corresponding to the groove depth of the compression stage jaws, to ensure maximal electrical contact while minimising the working distance during SEM imaging.

The sample geometry is shown in Figure 3.1 for both composites. The glass-PMMA samples were 4x2x3 mm^3 with the 2 mm width corresponding with the plate thickness [10]. The carbon-epoxy samples were 5x5x3 mm^3 with two semicircular notches drilled along the fibre orientation to localise strain [11]. As detailed earlier, both composites have different manufacturing methods, thus inducing these different geometries and V_f. As nano-DIC focuses on local fibre arrangement within the ROI, those differences should not compromise the comparability of the nano-DIC measurements between the two composites.

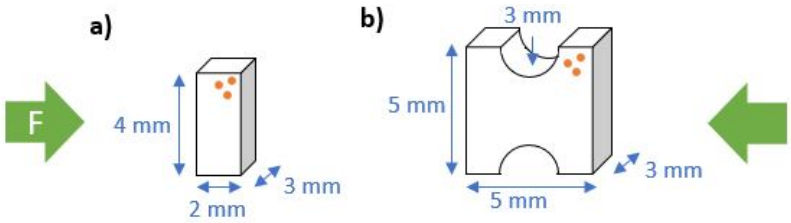

Figure 3.1: Geometry of the UD FRP composite samples for (a) GF-reinforced PMMA and (b) CF-reinforced epoxy.

3.1.4 Polishing of composite sample surfaces

All the samples for the two composites were polished perpendicular to the fibre orientation on a semiautomatic MultiPrep Precision Polishing System (Allied High Tech Products, Inc., California, USA). Diamond Lapping Film discs (Allied High Tech Products, Inc.) with successive roughnesses of 30-1 µm were used to grind the sample surface and those with successive roughnesses of 0.5-0.1 µm for finishing.

3.2 Speckle pattern deposition

A dense, homogeneous speckle pattern with particle diameters around 15 nm, shown in Figure 3.2, was generated at UCLouvain by the island growth (Volmer-Weber) deposition mode while aiming for a coating thickness of 5 nm. Indium, from pellets containing 99.99 % In, was deposited on the polished surface of the samples by e-beam evaporation with a deposition rate of 1 $Å s^{-1}$ under a pressure of $4x10^{-7}$ mbar. This method is based on the protocol of Hoefnagels et al. [52] for the deposition of nanometric DIC speckles onto metallic specimens by PVD [10].

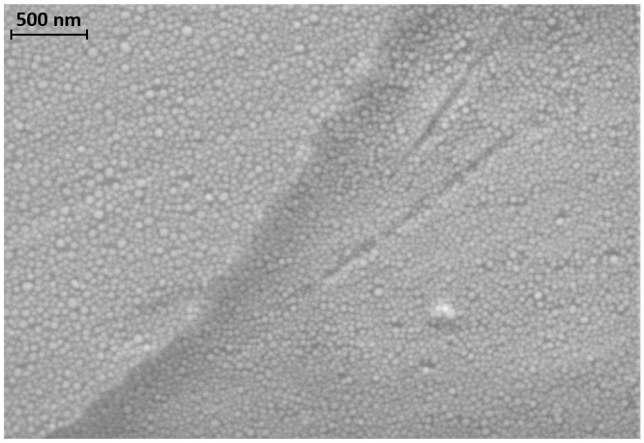

FIGURE 3.2: SEM micrograph of speckle pattern on glass-PMMA sample.

3.3 In-situ compression in Scanning Electron Microscope

To capture strain localisation areas, the samples were subjected to transverse compression in an Ultra 55 Field-Emission SEM (Zeiss, Germany) as this loading mode favours plasticity within the matrix [43].

3.3.1 Preparation of composite specimens for Scanning Electron Microscopy imaging

Polymer composites are poor electric conductors, which causes unwanted charging effects. Charging provokes unexpected contrast and is thus detrimental to image quality and consequently impacts the accuracy of the DIC. The conductivity of the sample was improved by subjecting the polished surface with the speckle pattern to carbon sputtering and coating all the other surfaces with silver [10].

3.3.2 Compression testing

The samples were mounted on a microtest compression stage equipped with a 2 kN load cell (Deben UK Ltd., UK) and inserted into the chamber of the SEM. The compression test consists of successive steps of 50-200 N until macroscopic failure occurs, which is expected somewhat below 2000 N. Large steps were taken in the beginning until cracks are expected, which is around 1000-1300 N, followed by smaller loading steps. The stage motor was stopped in between the steps to allow the sample to relax before imaging. The relaxation effect is negligible in the strain maps when the load drop is no more than 1 N in 1 min, as this is the average time to take two successive SEM micrographs [10]. The load-displacement curves are displayed in appendix A.2.

3.3.3 Acquisition of Digital Image Correlation data

The nano-DIC data was obtained by SEM imaging. At every load step, two successive images were taken, the second being for drift corrections, as will be explained in section "3.5.3 Drift correction". For each sample, up to three ROIs were chosen with interesting fibre configurations, which will be detailed in section "3.4 Fibre configurations". The size of the ROIs varies between 5.8x3.9 µm^2 and 22.5x15.2 µm^2 for corresponding magnifications between 20 000 x and 5 000 x. The acceleration voltage was set at 2 kV for the glass-PMMA composite and at 4 kV for the carbon-epoxy composite. The chosen voltage was adjusted between low values to limit charging and high values to intensify contrast. Charging was not entirely avoided, even with the coatings described in section 3.3.1. For adequate image quality with charging effects, the parameters for brightness and contrast were adapted during the compression test.

3.4 Fibre configurations

To compare the different ROIs in both composites, a categorisation was proposed. Three global fibre configurations are defined in Figure 3.3: horizontal (0°), vertical (90°) and diagonal (45°). Within this fibre configuration class, a matrix-fibre ratio was calculated to include the size effect of the matrix strip between the fibres. The non-dimensional matrix-fibre ratio was calculated by:

$$M/F = \frac{\text{matrix strip length}}{\text{fibre diameter}} \tag{3.1}$$

where M/F denotes the matrix-fibre ratio. The matrix strip length was measured with the open-source software ImageJ (National Institutes of Health, Maryland, USA) in µm. The nominal fibre diameter is 15 µm for the GFs and 7 µm for the CFs. More fibre configurations could be investigated including up to five fibres but this first analysis is limited to the most simple configurations with two fibres.

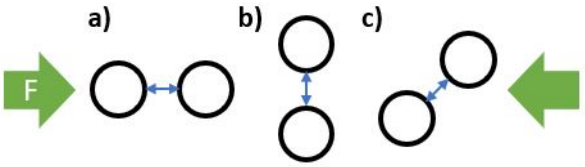

FIGURE 3.3: Analysed fibre configurations and their corresponding measured matrix strip in uniaxial compression (a) horizontal, 0° (b) vertical, 90° (c) diagonal, 45°.

3.5 Digital Image Correlation data processing

The speckle pattern displacements on the SEM micrographs were analysed with two different DIC software packages. A strain deviation analysis was performed to define their optimal set of input parameters. A drift correction was applied to the data to adjust for time-varying distortions.

3.5.1 Digital Image Correlation measurements

Two strain mapping software packages are proposed for the DIC analyses: the open-source software Ncorr and the VIC-2D software (7.2.0, Correlated Solutions Inc, South Carolina, USA).

Ncorr

Ncorr is a 2D subset-based DIC software package implemented in MATLAB (2018b, MathWorks, California, USA). The ROI on the reference image was divided into small round regions called subsets. This subset is a group of pixels in which the deformation, and hence strain, is assumed to be homogeneous. The measurement was based on software tracking the deformed subsets. The placement of two adjacent subsets was determined by a spatial shift in pixels named step size. The input values for the subset and step size quantify the spatial resolution of the calculated displacements. The strain radius, contrarily, impacts the level of numerical noise in the final strain maps. This input value indicates the size of the smoothing filter applied when converting displacement fields into strain fields. The strain radius size is expressed in data points with one data point corresponding to the step size. [10, 48]. The input parameters chosen in this study are a subset radius of 10 px, a step size of 2 px and a strain radius of 5.

VIC-2D

The VIC-2D system measures full-field, 2D displacement and strain data for mechanical testing on planar specimens. It includes DIC software for the correlation analysis of the entered images. The Area-of-Interest (analogy for ROI) selected on the reference image was divided into squared subsets. The subset size to be introduced is the width of the square (analogous to the subset radius in Ncorr). The

step size (similar to Ncorr) controls the spacing of the points to be analysed [60]. The correlation was run with a normalized squared differences criterion, an optimised 4-tap interpolation and Gaussian subset weights. Hencky strains were selected to be computed from the resulting displacements and smoothed with a 90% centre-weighted decay filter (corresponding to the strain radius in Ncorr) [50]. The input parameters chosen in this study are a subset size of 23 px, a step size of 2 px and a filter size of 15.

3.5.2 Strain deviation analysis

The strain deviation analysis described by Mehdikhani et al. [50] allows the evaluation of the optimal DIC input parameters. The suitable combination of input parameters for each software depends on the magnification and quality of the obtained SEM micrographs. Nano-DIC was applied to virtually deformed images to avoid the artefacts of experimental strains. The reference image was an SEM micrograph of an undeformed composite specimen with a size of 1024x768 pixels. The numerically deformed image was obtained by extending the same image with 10 pixels in the x-direction using the *lanczos3* resizing method in MATLAB (MathWorks). The theoretical strain is given by:

$$\varepsilon_{eng,x} = \frac{1034 - 1024}{1024} = 0.0098 \tag{3.2}$$

where $\varepsilon_{eng,x}$ is the engineering strain in the x-direction. The elongation consisted of 10 px and the initial width of 1024 px. DIC measurements between the original and stretched image were performed for different sets of subset size, step size and strain radius and the engineering uniaxial strains ($\varepsilon_{eng,x}$) were extracted. These strains were then compared to the expected theoretical strain calculated in equation 3.2. An optimal set of DIC input parameters should have a mean strain equal to the theoretical strain and a minimal standard deviation on the strain.

3.5.3 Drift correction

As mentioned in section 2.4.1, spatial distortions are not problematic at high magnification. Time-varying drift distortions, however, are a larger problem at the fibre/matrix level and thus need to be accounted for. At every load step, a stationary image pair was taken (section 3.3.3). The difference in displacement amplitude over the ROI between this image pair determines the image noise related to drift distortion. The approach chosen in this study to minimise the distortion in time corrected all images for reference drift. The DIC displacement maps from the second image at the reference state were subtracted from the first image at this stage, which yields displacement drift maps. Those horizontal and vertical displacement drift maps were then subtracted from all the actual DIC displacement maps, which yielded drift-free maps used for strain calculations [56].

3.6 Finite Element Analysis

FEAs were performed for CF-reinforced epoxy using the commercial software Abaqus (2021, Dassault Systèmes, France) [61] based on the FEA of Klavzer et al. [10]. The fibre configurations from section 3.4 were recreated in the model to compare the strain localisation patterns with the experimental nano-DIC results. Two fibre halves with a diameter of 7 µm were separated by a 0.001, 1, 2, 3 or 4 µm matrix strip, yielding respectively $M/F = 0.000$, 0.143, 0.286, 0.429 and 0.571. The uniaxial compression was recreated by constraining the left edge of the RVE in Figure 3.4 and displacing the right edge over -0.5 µm during 100 s. The mesh of the RVE consisted of 2D plane stress elements (CPS3) with an approximate element size of 0.005 μm^2.

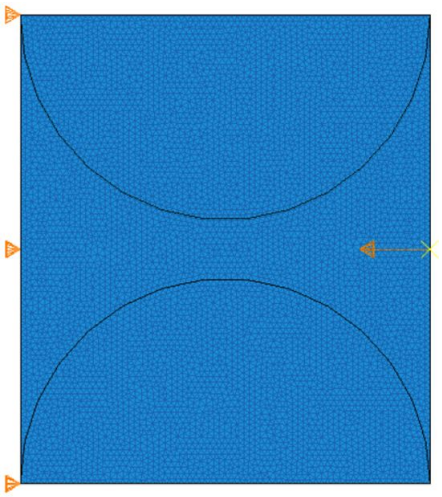

FIGURE 3.4: Finite element analysis for a vertical fibre configuration including the boundary conditions in orange indications and the mesh in grey.

The material properties of CF-reinforced epoxy are displayed in Table 3.1. The CFs were modelled as a linear elastic material and the thermoset epoxy matrix as a rate-dependent elastoplastic material. The pressure-dependent yield criterion for the matrix is a linear Drucker-Prager model to include the dependence of the polymer on the hydrostatic stress. This constitutive continuum model was identified and validated by Morelle et al. [62] for RTM6 and has a flow stress ratio of 1, a friction angle of 7.86° and a dilatation angle of 0°. The entire stress-strain hardening is included in appendix A.3. The interface between the fibre and matrix was assumed perfect and no damage mechanisms were included. The softening of the matrix induces convergence issues and therefore Abaqus Explicit with appropriate mass scaling was used instead of the standard Implicit computations.

	E_{11} [GPa]	E_{22} [GPa]	E_{33} [GPa]	ν_{12} [-]	ν_{23} [-]	ν_{13} [-]	ρ [g/cm^3]
CF	28	28	238	0.33	0.28	0.02	1.75
RTM6 matrix	3	3	3	0.34	0.34	0.34	1.14

Table 3.1: Material properties of carbon-epoxy composite: the Young's modulus E, the Poisson's ratio ν and the density ρ for the CF and the RTM6 epoxy matrix.

3.7 Strain fields

The mechanical behaviour at the fibre/matrix level is displayed in strain maps. The strain fields of interest were those of the image right before failure as this was where the strain localisation is the most definite. The experimental strains ε_{xx}, ε_{yy} and γ_{xy} were the calculated by Ncorr and VIC-2D. These strains correspond with the compression direction (x), the transverse direction (y) and the shearing (xy). Logarithmic, or Hencky, strains were chosen to be mapped with MATLAB (MathWorks). VIC-2D and Abaqus (Dassault Systèmes) provide logarithmic strains but Ncorr computes Lagrangian strains. For the sake of comparison of the results, the logarithmic strains were computed by:

$$\varepsilon_{log} = \frac{1}{2}\ln(2\varepsilon_{Lag} + 1) \tag{3.3}$$

where ε_{log} stands for the logarithmic strain and ε_{Lag} for the Lagrangian strain [5].

The principal strains enable the comparison of different systems by displaying the onset of plasticity independently of the loading direction. The first and second principal strains are the maximum and minimum normal strains, calculated by:

$$\varepsilon_{1,2} = \frac{\varepsilon_{xx} + \varepsilon_{yy}}{2} \pm \sqrt{\left(\frac{\varepsilon_{xx} - \varepsilon_{yy}}{2}\right)^2 + \left(\frac{\gamma_{xy}}{2}\right)^2} \tag{3.4}$$

where ε_1 and ε_2 denote respectively the first and second principal strain, and ε_{xx}, ε_{yy} and γ_{xy} the experimental strains in the compression, transverse and shearing direction [63]. The maximum shear strain was obtained by:

$$\gamma_{max} = 2\sqrt{\left(\frac{\varepsilon_{xx} - \varepsilon_{yy}}{2}\right)^2 + \left(\frac{\gamma_{xy}}{2}\right)^2} \tag{3.5}$$

where γ_{max} is the maximum shear strain and ε_{xx}, ε_{yy} and γ_{xy} the experimental strains in the compression, transverse and shearing direction [63].

As a reference for the global strain in the ROI, the macroscopic strain ε_{macro} was extracted from the load-displacement curve by:

$$\varepsilon_{xx,eng} = \frac{\Delta L}{L_0} \tag{3.6}$$

where $\varepsilon_{xx,eng}$ stands for the the engineering strain in the x-direction, L_0 for the initial length and ΔL for the change of length [63]. The displacement ΔL was measured by the load cell and the initial length L_0 was 2 mm for the glass-PMMA composite and 5 mm for the carbon-epoxy composite according to the sample geometry described in section 3.1.3. Note that this is merely an approximation for the carbon-epoxy composite as the local change in stress triaxiality due to the notches in the sample was not considered. This engineering strain was related to the logarithmic strain by:

$$\varepsilon_{log} = \ln(\varepsilon_{eng} + 1) \tag{3.7}$$

where ε_{log} stands for the logarithmic strain and ε_{eng} for the engineering strain [63]. Macroscopic stresses could also be extracted from the load-displacement curve by:

$$\sigma_{xx,eng} = \frac{F}{A_0} \tag{3.8}$$

where $\sigma_{xx,eng}$ stands for the the engineering stress in the x-direction, F for the applied force and A_0 for the initial cross-sectional area [63]. The force F was measured by the load cell and the initial cross-sectional area A_0 was 12 mm^2 for the glass-PMMA composite and 6 mm^2 for the carbon-epoxy composite according to the sample geometry described in section 3.1.3. The cross-sectional area in between the notches was chosen for the carbon-epoxy composite as this is where the stress is expected to concentrate.

Finally, the equivalent strain was introduced as a scalar to describe and compare any state of strains over different dimensions. It was obtained from the principal strains through:

$$\varepsilon_{eq} = \frac{2}{3}\sqrt{\varepsilon_1^2 - \varepsilon_1\varepsilon_2 + \varepsilon_2^2} \tag{3.9}$$

where ε_{eq} denotes the equivalent strain and ε_1 and ε_2 the principal strains [63]. In uniaxial compression, $\varepsilon_{eq} = \varepsilon_1$, which would correspond, for the macroscopic scale, to the values computed with equation 3.6.

Chapter 4

Results and discussion

This chapter presents the results from nano-DIC experiments and discusses the utility of nano-DIC to mechanically characterise polymer-based composites at the fibre/matrix level. First, a DIC software comparison will be elaborated to choose an optimal software. Secondly, strain localisation patterns around the fibres are examined. Then, the failure location in the ROI is analysed and submicron shear bands are examined. Furthermore, the experimental nano-DIC values are compared to the FEA. Finally, some recommendations for the use of nano-DIC are included. All the results present logarithmic strains unless stated otherwise.

4.1 Software comparison

The strain maps were obtained from the SEM micrographs through DIC software packages. Two software packages were introduced in section 3.5.1 and will be compared in the following section to select the best software for the image analysis. Both the input parameters and the underlying algorithm can affect the measured strain amplitudes and distributions, which will respectively be discussed in the results of the strain deviation analysis and the DIC comparison. Before entering the details, note that a one-to-one comparison is not accomplished. The correlation threshold and other software limitations prevented the comparison of equal subset areas for fully correlated images.

4.1.1 Strain deviation analysis

The optimal DIC input parameters for both software packages were obtained by the strain deviation analysis described in section 3.5.2. Various combinations of the three input parameters, i.e. subset size, step size and filter size were compared and the results are displayed in Figure 4.1. The optimal set of DIC input parameters correctly computes the mean strain $\mu(\varepsilon)$ of 0.0098 according to equation 3.2. The standard deviation σ around this mean strain, which is a measure of the strain non-uniformity is minimised [50]. For the sake of comparison between different data sets, the relative standard deviation or coefficient of variation $CV = \frac{\sigma}{\mu}$ will be used. As mentioned in

section 2.4.1, a trade-off between intensity and spatial resolution was made while favouring high spatial resolution to measure strain localisation. Larger subset size, step size and filter size include more data, which increases the intensity resolution since imperfections are averaged out. Larger data sets, though, lose spatial resolution because local variations are not captured.

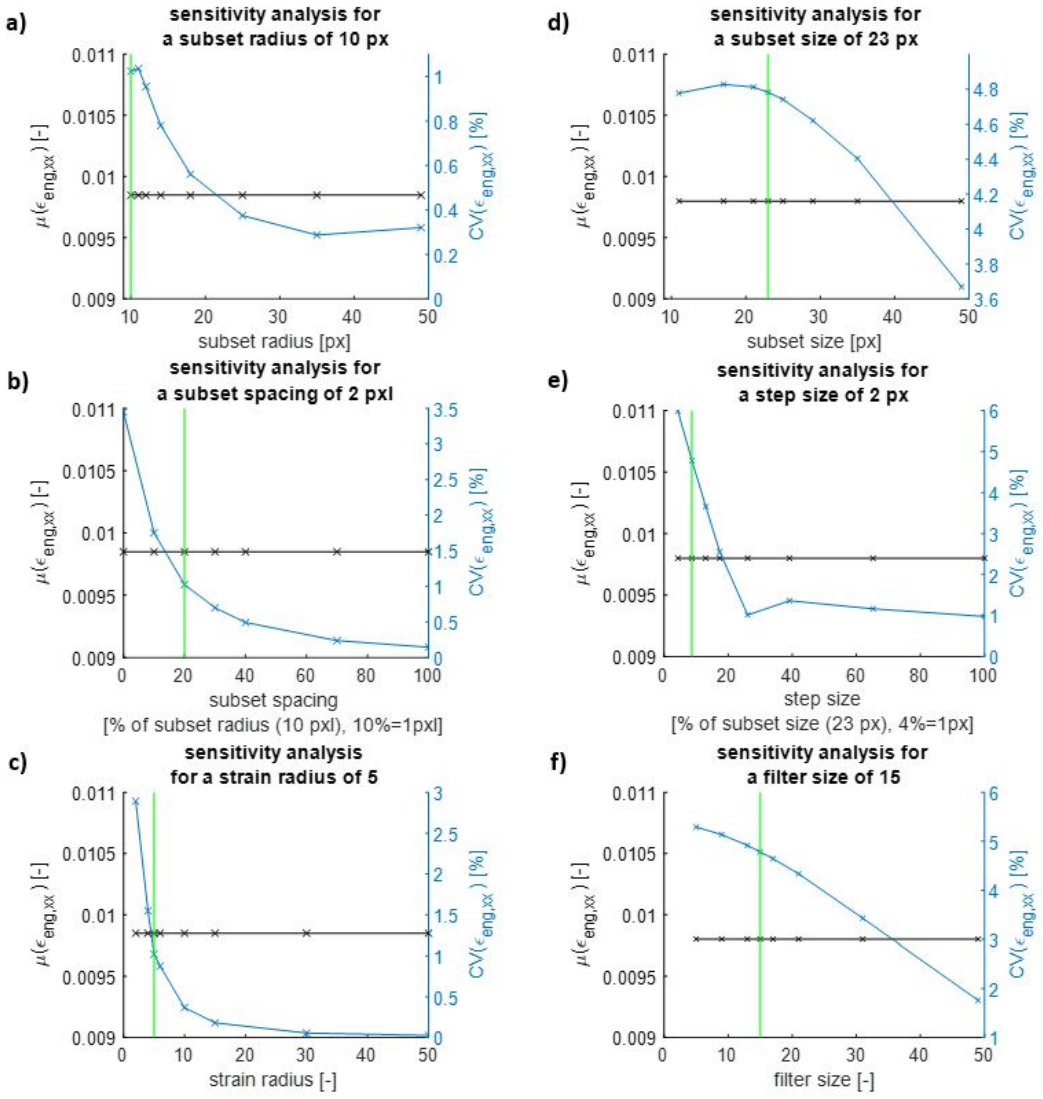

Figure 4.1: Sensitivity analysis for two DIC software packages: (a-c) Ncorr and (d-f) VIC-2D. The analysis varies around (a) a 10 px subset radius, (b) a 2 px subset spacing, (c) a strain radius of 5, (d) a 23 px subset size, (e) a 2 px step size, and (f) a filter size of 15.

Ncorr

For Ncorr, the optimal set of parameters was a 10 px subset radius, a 2 px subset spacing and a strain radius of 5 [10]. Each input parameter was varied while keeping the other two constant at these optimal values. The strain deviation analysis on the subset radius in Figure 4.1a showed increasing the subset radius decreases the CV and thus lowered the intensity noise. The larger subsets hold more speckles, which facilitates the subset recognition for the algorithm. The optimal subset radius was set to 10 px, which is the smallest option in Ncorr. A subset area of 314 px^2 was thus opted for. This enables the highest possible resolution for an acceptable intensity in noise distribution of $CV = 1.02$ %.

The strain deviation analysis on the subset spacing in Figure 4.1b demonstrates that increasing the subset spacing decreases the CV and simultaneously the intensity noise. A lower step size allows the analysis of more pixels, which yields more detailed correlations. The optimal subset spacing was set to 2 px, which is 20 % of the optimal subset radius. This enables, similarly to the subset radius, the highest possible resolution for an acceptable $CV \approx 1$ %.

The strain deviation analysis on the strain radius in Figure 4.1c presents that increasing the strain radius decreases the CV as the noise on the resulting strain is reduced by smoothing. The optimal strain radius was set to 5, which includes 10 px, to enable, again, the highest possible resolution for an acceptable $CV \approx 1$ %.

VIC-2D

For VIC-2D, the optimal set of parameters was a 23 px subset size, a 2 px step size and a filter size of 15 [50]. The same subset size as for Ncorr (10 px) was not selected because VIC-2D suggests a subset size based on the input, contrarily to Ncorr. For the three input parameters, the CV-value decreases with increasing parameter size. Figure 4.1 reveals Similar trends as for Ncorr, having thus to choose an optimal value while balancing intensity and spatial resolution. The order of CV was however much higher than for Ncorr and thus for VIC-2D a $CV = 4.78$ % was assumed as acceptable. The subset size of 23 px corresponds to a subset area of 529 px^2, the step size of 2 px is 8 % of the subset size and the filter size of 15 holds 30 px.

4.1.2 Digital Image Correlation comparison

The same set of images was analysed with the two software packages. The obtained shear strain maps are displayed in Figure 4.2 and appendix B.1 includes the same strain fields as displayed in the respective software interfaces. The corresponding range of strain values is included in appendix B.2. For both a carbon-epoxy and a glass-PMMA composite, the three strain maps, i.e. ε_{xx}, ε_{yy} and γ_{xy}, showed similar patterns on the same scale. The data ranges revealed that the mean strain values of the map are almost equivalent. Averaged over the three strain maps and both composites, VIC-2D computed a relatively 4.2 % lower mean strain than Ncorr

in absolute value. The standard deviation depicts the dispersion of the data and exposed for VIC-2D a 9.1 % lower relative distribution of the strain values around the mean compared to Ncorr. The smaller dispersion of VIC-2D can be related partially to the larger subset area (529 px^2 vs. 314 px^2) not capturing the local variations. The filter size also affects the dispersion as VIC-2D uses a larger filter (30 px vs. 10 px) and smoothens the peak strain values out more than Ncorr. Besides demonstrating the DIC input parameter effects, this DIC software comparison could indicate that, at first sight, no algorithm-related errors were captured in terms of strain localisation areas.

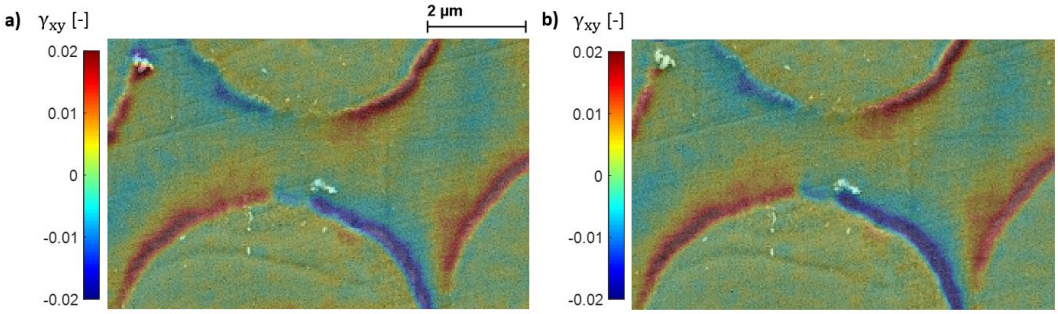

Figure 4.2: Shear strain map obtained by (a) Ncorr and (b) VIC-2D. The ROI includes a vertical fibre configuration of a carbon-epoxy composite with $M/F = 0.24$ and $\varepsilon_{xx,macro} = -0.047$.

4.1.3 Ncorr as optimal software

Based on the strain deviation analysis of section 4.1.1 and the DIC comparison of section 4.1.2, Ncorr was chosen as the optimal software and will be used throughout the rest of this master's thesis. Both software packages correctly compute average strains and are able to reveal strain localisation. Ncorr has the advantage that smaller intensity noise distributions were measured ($CV = 1.02$ % vs. 4.78 %) while capturing local variations with the smaller subset size (314 px^2 vs. 529 px^2).

4.2 Strain localisation around fibres in nanoscale strain maps

Nano-DIC could successfully capture strain localisations at the fibre/matrix level (Figure 4.3). Localised areas of large strain values were noticed around the fibres for all three fibre configurations from section 3.4 and in all the strain fields from section 3.7 for both the glass-PMMA and the carbon-epoxy composite. The normal strain concentration trends for ε_{xx} and ε_{yy} are elaborated below, whereas γ_{xy} and γ_{max} will be detailed respectively in sections "4.4.1 Submicron shear band pattern in shear strain maps" and "4.3.1 Prediction of failure location in maximal shear strain maps". A clear distinction is observed between the fibre and the matrix response.

The fibres have near-zero strain and are thus almost not deforming during the compression. The fibres are much stiffer than the matrix causing the matrix to carry the deformation as explained in section 2.3. At the matrix/fibre interface, a distinct strain gradient is visible and the smoothening of µDIC, mentioned in section 2.4.1, was overcome. This strain gradient was related to the interphase region between fibre and matrix, as mentioned by Klavzer et al. [10].

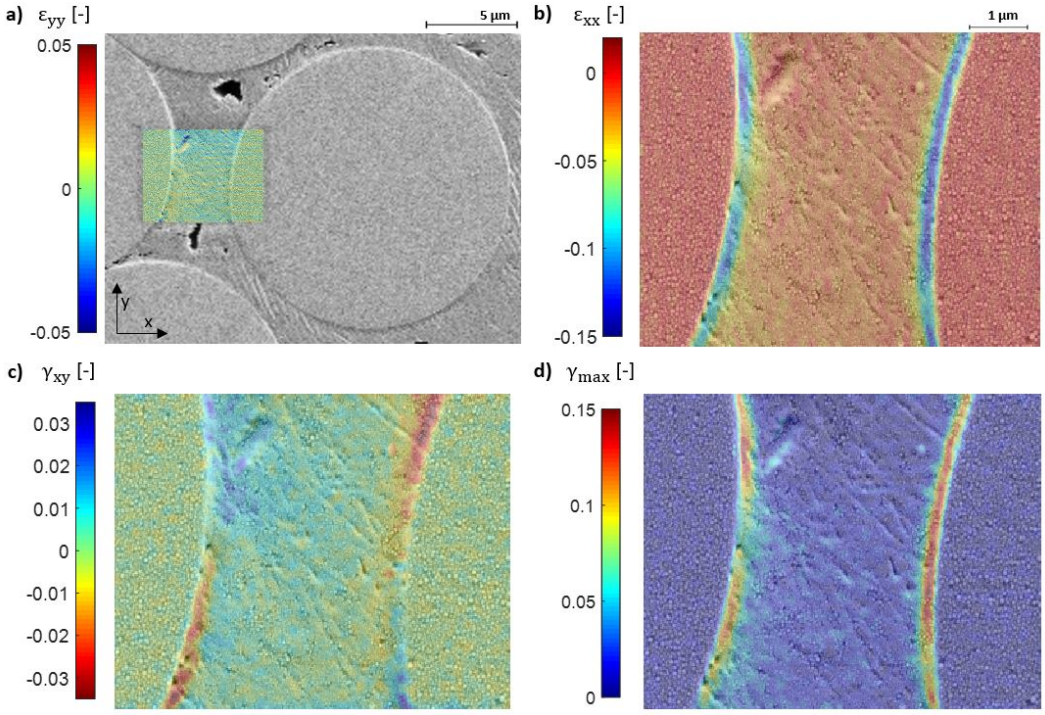

FIGURE 4.3: Strain localisation around fibres in nanoscale strain maps: (a) transverse strain in y-direction (b) transverse strain in x-direction (c) shear strain (d) maximal shear strain. The ROI includes a horizontal fibre configuration of a glass-PMMA composite with $M/F = 0.24$ and $\varepsilon_{xx,macro} = -0.137$.

Compressive strain concentrations along the direction of compression were systematically observed along the perpendicular fibre interface in all three fibre configurations. An example is given in Figure 4.3b and other results are included in appendix C.1. No obvious trends for the transverse strain localisation in the y-direction were detected, e.g. in Figure 4.3a.

Note on principal strains

The principal strains ε_1 and ε_2 were mapped to enable the comparison of different systems by displaying the onset of plasticity independently of the loading direction. An example of such strain maps is given in Figure 4.4 and appendix C.2. Overall,

similar patterns were observed for the ε_1-map as for the ε_{yy}-map and for ε_2 and ε_{xx}. In some ROIs, the mean strain value of the principal map differed significantly from that of the corresponding strain map. The dissimilarity could be related to the strain triaxialities created by certain groups of fibres. It could be expected that the patterns of the principal strain maps resembled those of the experimental normal strain directions. The minimum principal strain ε_2 is the highest compressive strain and the applied compression is along the x-direction. Likewise, the maximum principal strain ε_1 is expected perpendicular to the compression direction due to the plain stress effect, which corresponds with an expansion in the y-direction. The principal strain maps thus bring no new insight into strain localisation and hence will not be shown during the rest of this study.

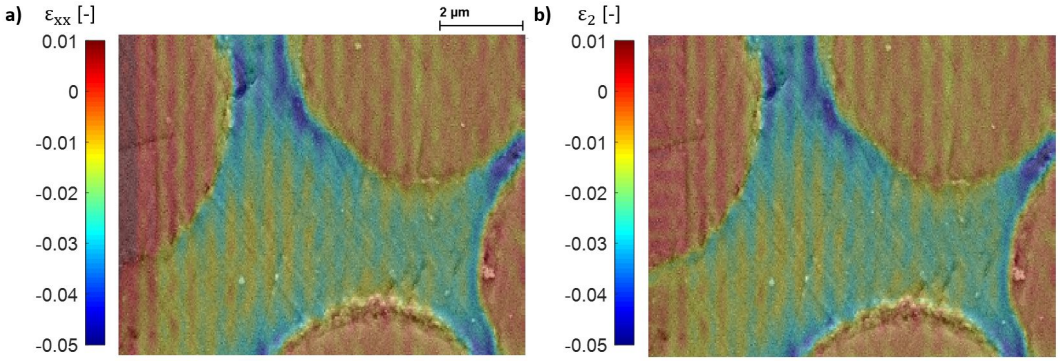

Figure 4.4: Comparison of principal and normal strains: (a) normal transverse strain map and (b) minimum principal strain map. The ROI includes a vertical fibre configuration of a carbon-epoxy composite with $M/F = 0.34$ and $\varepsilon_{xx,macro} = -0.055$.

4.3 Failure location in Region Of Interest

Local failure was captured inside the ROIs by crack appearances. The damage mechanisms are related to strain localisation in the matrix (section 2.3.2). The following sections will link the failure locations to the strain maps obtained by DIC, compare the local fracture strains to macroscopic ones, and analyse post-mortem SEM micrographs of the fracture surface.

4.3.1 Prediction of failure location in maximal shear strain maps

The failure locations, i.e. crack appearances, in the ROI could be pre-emptively identified via concentrations of maximal shear strain values. Maximal shear strain localisations were seen to coincide with the failure locations for the three fibre configurations in both composites. An example is given in Figure 4.5, where high maximal shear strain values were localised between the upper right and middle right fibres. The next load increment induced the crack to propagate from in between these fibres across the ROI. More predictions of failure location in maximal shear strain maps are included in appendix D.1.

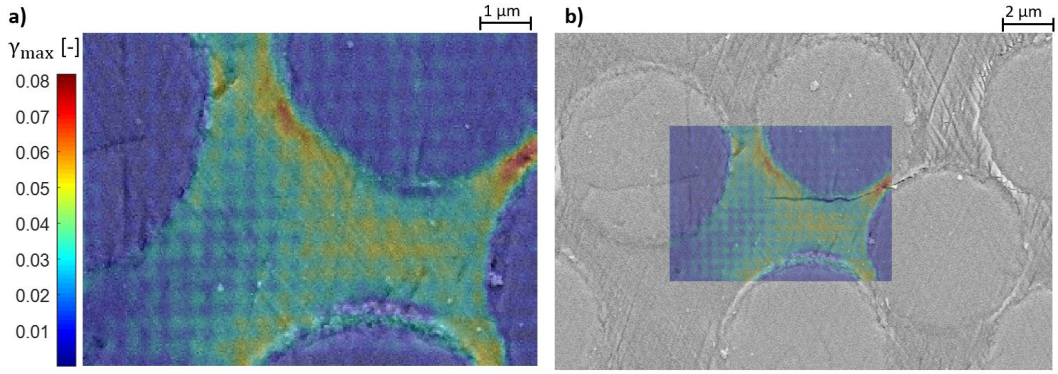

FIGURE 4.5: Prediction of failure location in maximal shear strain map: (a) maximum shear strain map before failure in ROI and (b) ROI location in between fibres after failure. The ROI includes a vertical fibre configuration of a carbon-epoxy composite with $M/F = 0.34$ and $\varepsilon_{xx,macro} = -0.055$.

4.3.2 Local failure strains compared to bulk strains

The previous section showed that maximal shear strain maps could predict the failure location. The question now arises if there is a critical value related to this. As failure starts at high maximal shear strain concentration, the maximum γ_{max} is suggested as a critical value. Once the crack entered the ROI, the DIC algorithm could no longer compute strains. The critical value was thus estimated in the load step right before local failure. One failed ROI was captured for the carbon-epoxy composite with a maximum γ_{max}-value of 8.2 %. Three failed ROIs were captured for the glass-PMMA composite with a mean maximum γ_{max}-value of 10.4 % and a CV of 33.8 %. The local strains depend strongly on the fibre configurations and nearby defects and the data set is too small to identify a real critical value. Also, no statistically significant difference was found between the maximum γ_{max}-value of both composites. Once again, the amount of data is too small to allow any strong conclusions on the material dependency of the maximum γ_{max}.

The local strain at failure in the ROI was then compared in Figure 4.6 to the macroscopic strain at failure in the ROI and to the macroscopic strain at the final failure of the sample by means of equivalent strains (equation 3.9). The local strain at failure in the ROI was obtained from the strain state in the nano-DIC map at the location of the maximum γ_{max}. The macroscopic strains were computed from the displacement measured by the load cell during compression (equation 3.6). Even though the glass-PMMA composite generated higher equivalent strains, both composites showed a similar trend, i.e. the macroscopic strain at local failure was somewhat higher than the local strain and the macroscopic strain at final failure was even higher. No significant difference was found in local failure for the local strain and macroscopic strain. This could possibly indicate that the local strain concentrations in the matrix govern the macroscopic behaviour of the composite in

transverse compression. The macroscopic strain at final failure is significantly higher than the strains at local failure. This could illustrate the ability of composites to accumulate damage. Note that no strong conclusions could be made for these strains since not enough data is included and the compliance of the load cell, as well as the notches in the carbon-epoxy samples, were not taken into account.

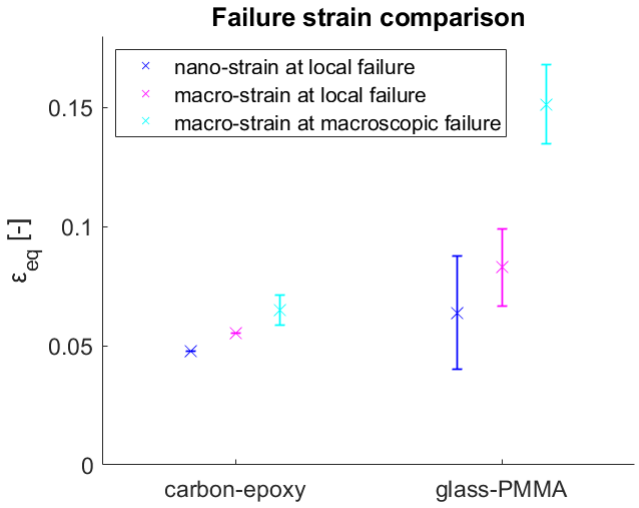

Figure 4.6: Equivalent failure strain comparison.

Previous research was already conducted on the carbon-epoxy composite by Chevalier [5] and on the glass-PMMA composite by Gayot [64]. The failure strains obtained were compared to their data in Figure 4.7. Both performed transverse compression tests on cubic UD specimens and measured the stress-strain response. Chevalier et al. [11] obtained a logarithmic failure strain of about 5.02 % and Gayot et al. [64] of 10.00 %. The experimental macroscopic strains at final failure of the sample of both composites exceed the respective failure strains from the literature, partly due to the exclusion of the compliance of the load cell, the notches in the carbon-epoxy samples and the edge effects of the contact points with the load cell. For the carbon-epoxy composite, the local failure strains matched with the macroscopic failure strain from the literature and it could be that something is triggering failure at a certain strain level independently of the scale. For the glass-PMMA composites, the local failure strain approximated the macroscopic yield strain rather than the failure strain. Those composites were manufactured by pultrusion, which induced lots of voids in the PMMA matrix. These defects were creating stress concentrations and triggering premature local failure. Overall, this comparison with the literature showed that the obtained failure strains are of acceptable size but their computation could be improved to continue the search for this critical value.

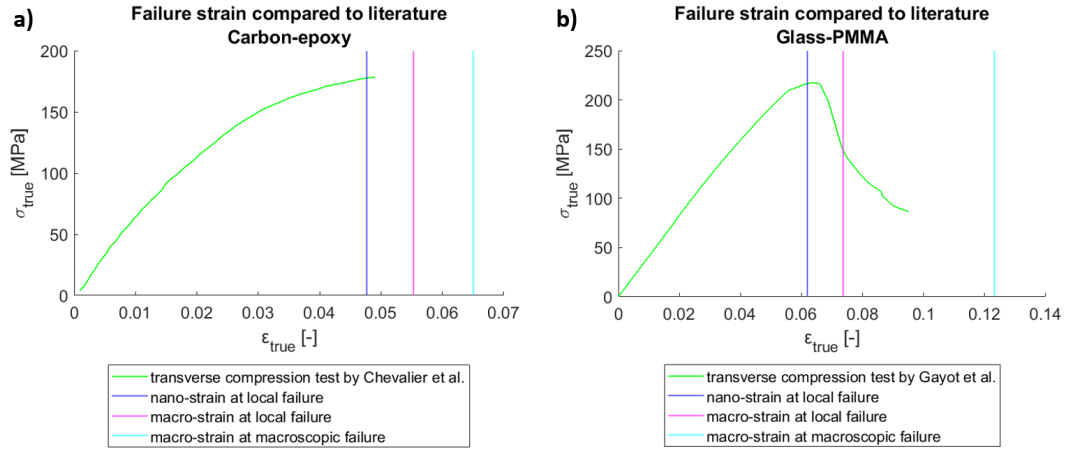

FIGURE 4.7: True failure strains compared to the macroscopic stress-strain response of UD cubic composite specimens in transverse compression from literature: (a) carbon-epoxy with results from Chevalier et al. [11] at a strain rate of 10^{-4} s^{-1} and (b) glass-PMMA with results from Gayot et al. [64]

The previous paragraph demonstrated an overestimation of the computed failure strains, therefore, a second approach was proposed for the calculations and these results are displayed in Figure 4.8. The preceding failure strains were calculated from the displacements measured by the load cell (equation 3.6) and the new approach was based on the measured loads (equation 3.8). These forces were related to stresses and then the stress-strain curves from earlier research [11,64] associated strain values. The load-based strains were an underestimation of the failure strains and the strain computation could still be improved.

Neither the displacement-based approach nor the force-based approach for the macroscopic strains seemed to fit the data from the literature. The local failure strain was expected to be higher than the macroscopic strain at the final failure because the sample holds more defects than the ROI. This was the trend observed for the force-based approach but those macroscopic strains were a large underestimation of the literature. The displacement-based approach overestimated the failure strains but matched them much better. The reality is expected in between both strain computation approaches. Note that the sample design for the carbon-epoxy composite could be challenged. The main cracks appeared to rise from side effects of the coating and the clamping rather than the stress concentration in between the notches, giving rise to premature final failure. The local strain at local failure could also be questioned, as the choice of ROI is rather arbitrary. An unlucky choice in ROI could have been made, one with much more deformation in between the neighbouring fibres for example. The local strains were computed from the nano-DIC before local failure and are thus an underestimation. Also, the e-beam of the SEM affected the ROI by inducing some increased temperature effects on the matrix properties or even degrading the surface.

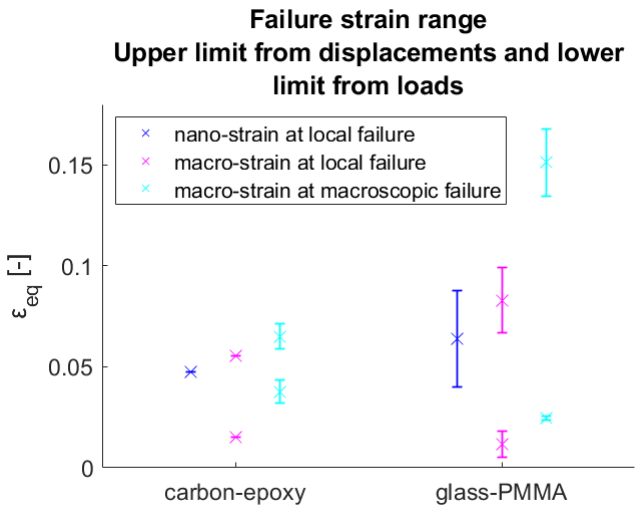

Figure 4.8: Equivalent failure strain results from both displacement and load calculations.

Chevalier et al. [65] also provided data on the equivalent fracture strain as a function of the mean stress triaxiality for carbon-epoxy specimens. The fracture strain decreased with increasing stress triaxiality and locally lower failure strains were observed, justifying thus locally more extreme stress conditions. For the local failure strain at local failure, a stress triaxiality of 0.54 was obtained from the literature data, displayed in Figure 4.9. This is almost the stress triaxiality of biaxial tension, i.e. 0.66 and could be possibly explained by the splitting of the interface between fibre and matrix at this local scale.

4.3.3 Failure mechanisms observed in SEM micrographs

As mentioned in section 2.3.2, TP and TS matrices present dissimilar damage evolution behaviour. Klavzer et al. [10] demonstrated that the glass-PMMA composite displays ductile behaviour and the carbon-epoxy composite behaves in a brittle manner. Fracture surface images on several length scales are included in Figure 4.10 and appendix D.2. The glass-PMMA composite showed signs of damage accumulation over the entire surface before failing after entering global plasticity. Strong plastic deformation in the matrix, via crazes and micro shear bands in between fibres, was observed. The crack appeared to open in the matrix and led to interface debonding when reaching a fibre. The carbon-epoxy composite showed signs of sudden failure with macroscopic cracks propagating along the fibre/matrix interface. In the ROI, failure occurred via interface debonding. For both composites, microscopic cracks in the conductive coating were noticed in a diamond grid pattern, confirming nano or micro shear band formation for the matrix below. Note that these observed differences in fracture surfaces may also be related to the different specimen geometry (section 3.1.3), leading to different stress concentrations.

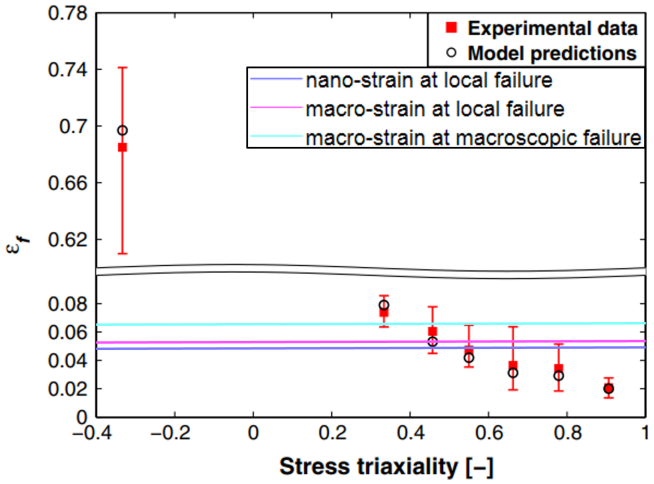

FIGURE 4.9: Failure strain results compared to the equivalent fracture strain as a function of the mean stress triaxiality for carbon-epoxy. Adapted from [65].

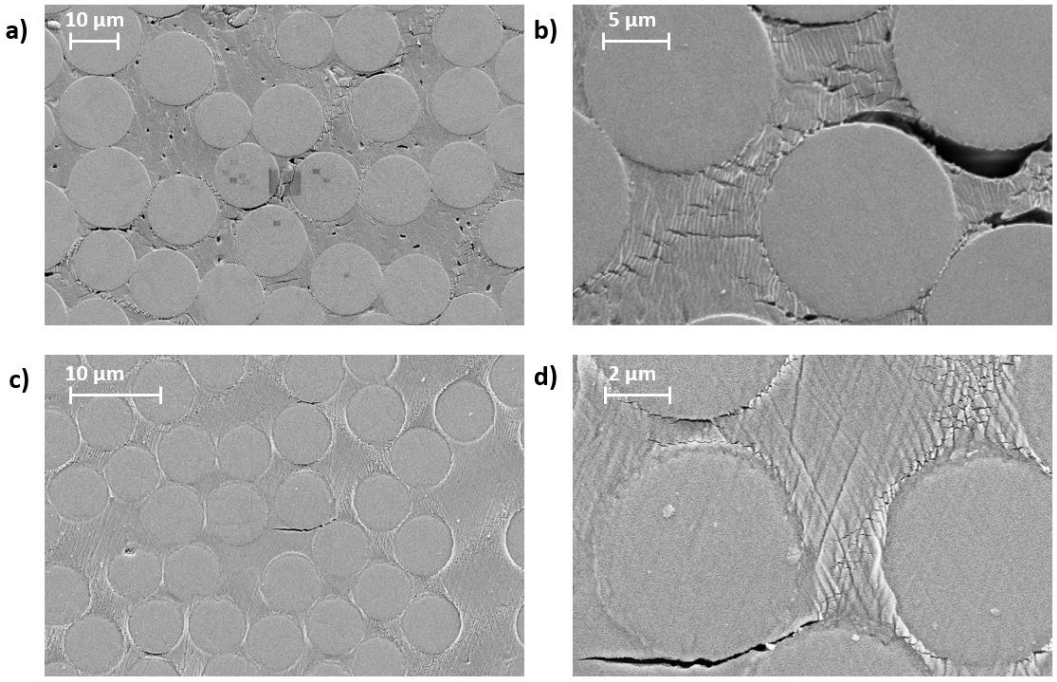

FIGURE 4.10: Post-mortem observations of the failed material surface: (a-b) glass-PMMA and (c-d) carbon-epoxy composite.

4.4 Submicron shear bands

In section 4.2, strain localisation areas around the fibres in shear strain maps captured by nano-DIC were introduced. X-shaped patterns were recognised (appendix E.1) and linked to shear bands (Figure 2.4). The following sections will elaborate on the submicron shear band pattern, the shear band evolution with increasing strain and the shear band orientation.

4.4.1 Submicron shear band pattern in shear strain maps

The formation of local submicron shear bands was captured for both composites in the resulting shear strain maps for all three configurations. The shear bands were found between two fibres oriented along the matrix strip as defined in Figure 3.3. An example of the shear strain map is given in Figure 4.11, which compares a nano-DIC strain map with an FE prediction. Figure 4.2 and Figure 4.3c also display submicron shear bands. The shear bands did not propagate through the matrix strip in between the fibres and remained localised at the fibre/matrix interface. From the experimental data, it could be assumed that the strain localisation induced the interface to fail before the shear band could propagate. The FEA, on the contrary, did not include failure criteria and the shear bands still did not propagate (validated up to 5 % applied compressive strain). The presence of shear bands indicated the strain-softening behaviour of the matrix (section 2.2.2), even when confined in between fibres. Qualitatively, the local shear behaviour of the matrix thus seemed to resemble the X-shaped shear band pattern of the bulk matrix behaviour (Figure 2.4).

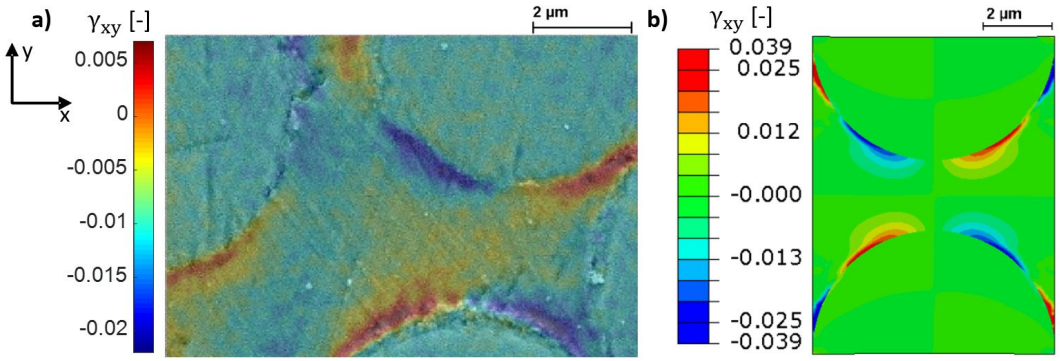

Figure 4.11: Shear strain maps for a vertical carbon-epoxy configuration at $\varepsilon_{xx,micro} = -0.013$: (a) nano-DIC map for an ROI with $M/F = 0.34$ and $\varepsilon_{xx,macro} = -0.055$ and (b) FEA for a model with $M/F = 0.29$.

4.4.2 Submicron shear band evolution with increasing strain

Taking images at consecutive load steps (section 3.3.3), allowed picturing the strain localisation with increasing compression. An example of such a series of nano-DIC maps is displayed in Figure 4.12. The strain localisation patterns appeared to

enhance. FEA also captured these enhancements, included in appendix E.2, during increased loading as well as by varying M/F. The strain localisation enhancement depended on the fibre configurations and the orientation of the shear band base (defined in appendix E.1), as will be detailed below.

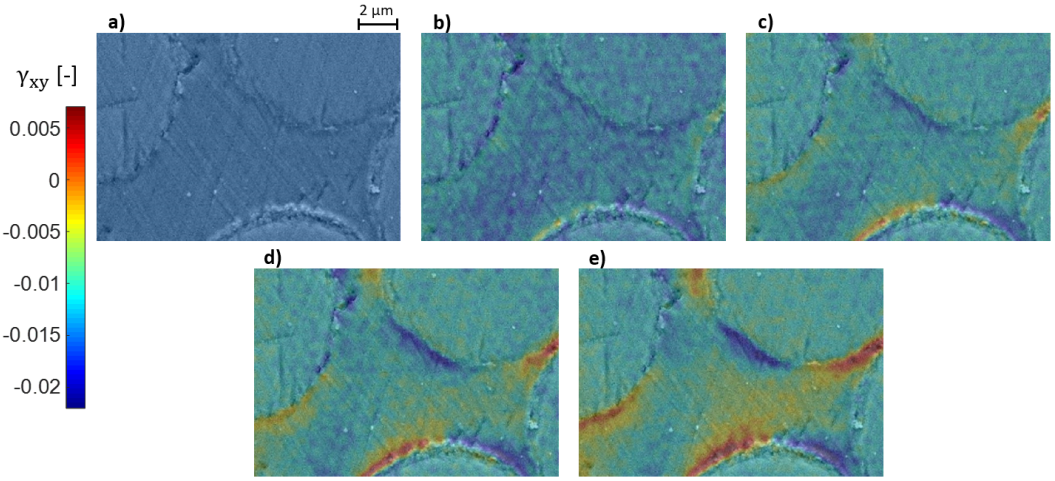

FIGURE 4.12: Shear strain maps evolving with increasing compressive strain. The ROI includes a vertical fibre configuration of a carbon-epoxy composite with $M/F = 0.34$ and $\varepsilon_{xx,macro}$ = (a) -0.017, (b) -0.034, (c) -0.041, (d) -0.048 and (e) -0.055.

In the horizontal fibre orientation, increasing the compressive load brought the fibres closer together, thus lowering M/F. The shear bands appeared to grow by increasing strain amplitude and broadening along the fibre/matrix interface (Figure 4.13). It could be argued that the shear bands are stretched by the transverse tensile strain oriented along the shear band base.

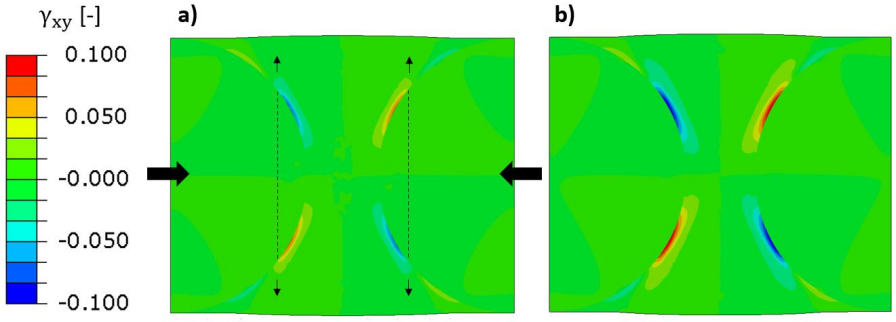

FIGURE 4.13: Growing shear bands in FEA shear strain map of horizontal fibre configuration of a carbon-epoxy composite with $M/F = 0.29$: (a) $U_x = -0.20$ µm and (b) $U_x = -0.25$ µm.

In the vertical fibre orientation, increasing the compressive load corresponds to driving the fibres further away and thus increasing M/F. The shear bands appeared to intensify in strain amplitude at a fixed position (Figure 4.12 and Figure 4.14). Similarly, it could be reasoned that the transverse tensile shear strain is now oriented perpendicular to the shear band base and no longer stretching the shear band base.

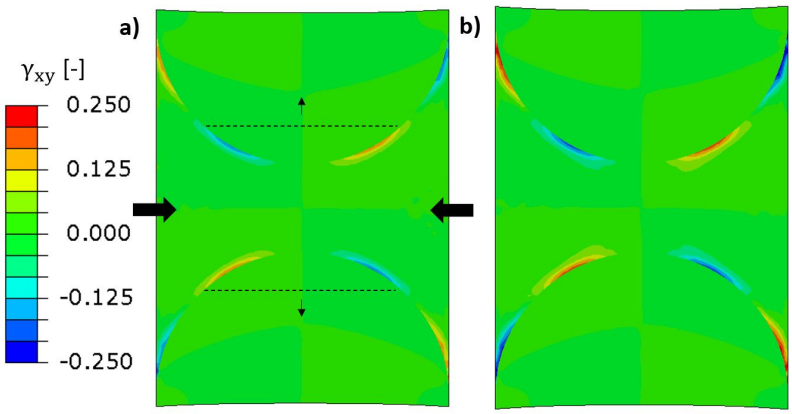

Figure 4.14: Intensifying shear bands in FEA shear strain map of vertical fibre configuration of a carbon-epoxy composite with $M/F = 0.29$: (a) $U_x = -0.20$ µm and (b) $U_x = -0.25$ µm.

In the diagonal fibre orientation, a combination of the growing horizontal and intensifying vertical cases was obtained. In Figure 4.15, the positive shear strain zones can be seen growing along the transverse tensile strain and the negative shear strain zones intensifying perpendicular to the transverse tensile strain.

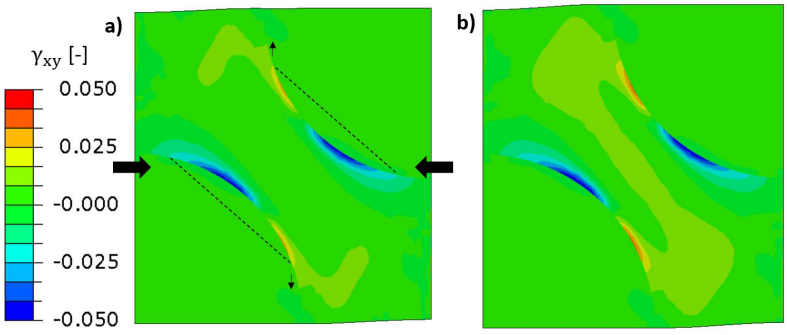

Figure 4.15: Growing and intensifying shear bands in FEA shear strain map of diagonal fibre configuration of a carbon-epoxy composite with $M/F = 0.29$: (a) $U_x = -0.20$ µm and (b) $U_x = -0.25$ µm.

4.4.3 Submicron shear band orientation in vertical fibre configuration

In the previous section, the shear bands were noticed to intensify in the vertical fibre configuration. Their evolution with increasing matrix strip length was studied for the angle, base and orientation. Several M/F designs were examined for both FEA and DIC. Figure 4.16a shows that the shear band angle decreased when the fibres are further away. The shear band base trend was analysed to account for a possible geometry effect and is shown in Figure 4.16b. The shear band base length increased with the matrix strip length and it thus seemed that the local fibre configuration governs the shear band dimensions. Both trends illustrate that the FEA systematically overestimated the nano-DIC values.

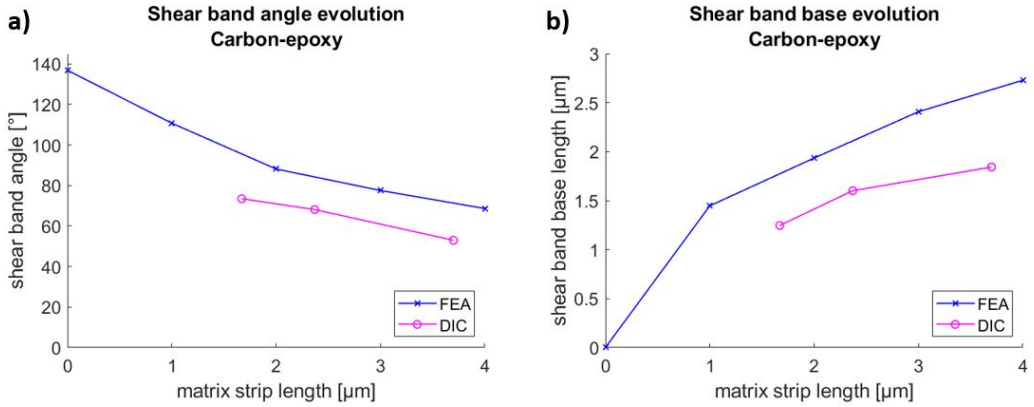

FIGURE 4.16: Shear band trend with increasing matrix strip length for a vertical carbon-epoxy configuration: (a) the shear band angle evolution and (b) the shear band base evolution. A comparison of FEA with varying M/F at $U_x = -0.075$ µm is made with nano-DIC for 3 ROIs right before their respective failure.

The shear band orientation respective to the loading direction increased with the matrix strip length (Figure 4.17). In section 2.3.2, a shear band orientation ranging from 52.5° for a pure matrix to 60.0° depending on the fibre volume fraction [22], was found and is also included in Figure 4.17. The nano-DIC data appeared to correspond better with this range. Larger matrix strip lengths matched better with the range from the literature, showing that a less confined matrix resembles the bulk matrix more. The FEA trend is 16.2 % lower than the nano-DIC trend on the orientation. This large discrepancy is an indication of a clear difference between the in-situ matrix properties and the bulk properties used in the FEA. Remark that part of the discrepancy is probably related to the limitations of the model, i.e. boundary conditions, edge effects, approximated geometry, etc.

The yield stress in the Drucker-Prager hardening law was increased by 20 % over the entire strain softening and hardening regime (appendix E.3) to assess the effect of the input values of the FEA on the shear band orientation. The strain maps in

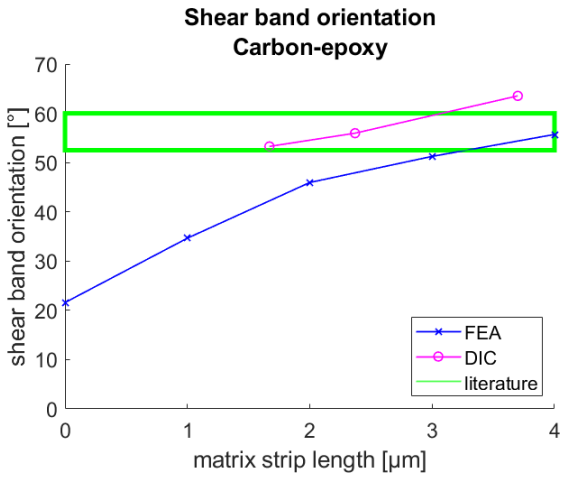

Figure 4.17: Shear band orientation with respect to the compressive loading direction varying with the matrix strip length for the carbon-epoxy composite. A comparison of FEA with varying M/F at $U_x = -0.075$ µm, nano-DIC for 3 ROIs right before their respective failure, and the shear band orientation range by Hu et al. [22].

Figure 4.18 displayed that slightly lower strain localisations were obtained for the delayed onset of plasticity in the carbon-epoxy composite with $M/F = 0.286$. The shear band orientation decreased by 4.7 % compared to the original hardening law and the FEA trend on the orientation was 19.7 % lower than the nano-DIC trend (vs. 16.2 % for the original hardening law). An indication towards locally lower yield stress could be seen but the difference in the shear band orientation is almost insignificant for an increase of 20 % of the hardening. That no extreme difference in the pattern was obtained could already be expected because of the similar patterns in glass-PMMA and carbon-epoxy, which have different matrix properties.

4.5 Comparison between experimental values and Finite Element Analysis

The observed patterns of nano-DIC were compared to an FEA based on constituent properties validated at the macroscale. A model with corresponding fibre orientation and M/F was contrasted with a carbon-epoxy ROI at equal applied microscopic compressive strain. The model results revealed similarities and inconsistencies with the nano-DIC results (Figure 4.11 and appendix F.1). The strain localisation patterns from nano-DIC (section 4.2) could be recognised in the FEA maps. The shear bands of the FEA showed however an alternating strain sign on one-quarter of the fibre, which did not appear in the experimental results. This discrepancy could be related to the small mesh elements and boundary effects on this tiny matrix zone in between the fibre and the boundary of the RVE. Also, the inability of DIC to

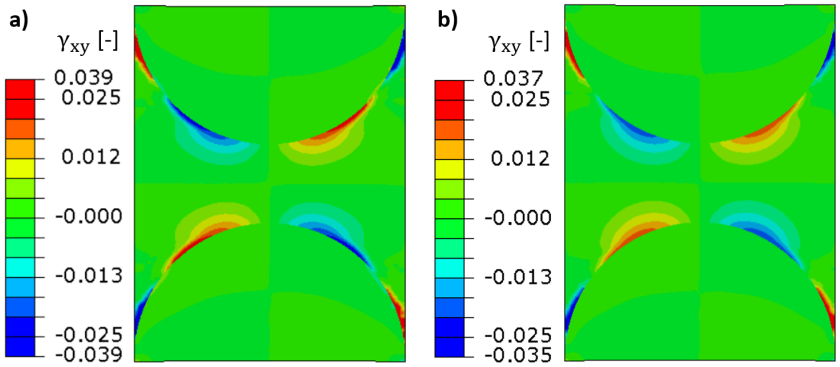

FIGURE 4.18: Effect of hardening on shear strain maps obtained by FEA for a vertical carbon-epoxy configuration with $M/F = 0.286$ and $U_x = -0.075$ µm: (a) original Drucker-Prager model by Morelle et al. [62] and (b) Drucker-Prager model increased by 20 %.

capture out-of-plane displacement, which will be detailed in section "4.6.2 Restriction due to out-of-plane deformation", led to differences between FEA and nano-DIC. Further research should be conducted on a wider model with larger matrix strips on the left and right of the fibre to differentiate the model effects from the material properties. Compressive strain concentrations along the direction of compression were systematically observed along the perpendicular fibre interface for both FEA and nano-DIC. Earlier, no obvious trends for the transverse strain localisation in the y-direction were detected in DIC. In Figure 4.19, FEA hinted at an hourglass-shaped localised strain area for the matrix in between the fibres. By re-scaling the nano-DIC results this pattern was recognised in two ROIs.

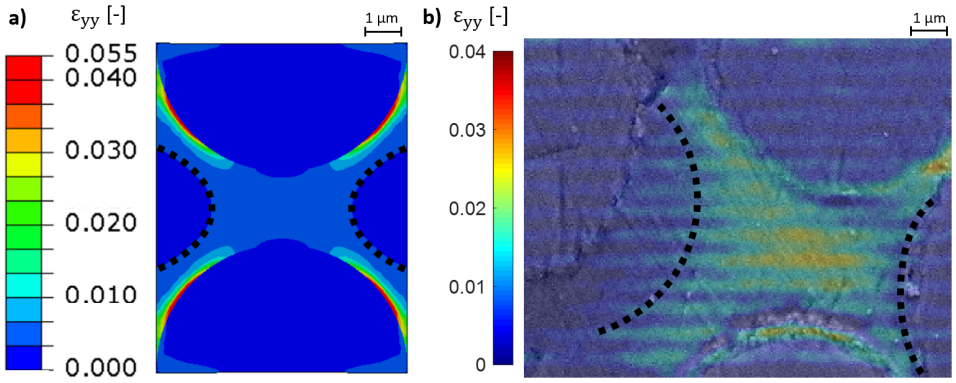

FIGURE 4.19: Transverse strain maps in the y-direction for a vertical carbon-epoxy configuration at $\varepsilon_{xx,micro} = -0.013$. The black dotted lines indicate the hourglass-shaped localised strain area. (a) FEA for a model with $M/F = 0.29$ and (b) nano-DIC map for an ROI with $M/F = 0.34$ and $\varepsilon_{xx,macro} = -0.055$.

Similarly as discussed for the submicron shear bands in section 4.4, the FEA qualitatively mimics the local mechanical behaviour of the matrix. The in-situ matrix properties thus seemed to resemble the macroscopic ones since both yield similar strain localisation patterns. Quantitatively, the FEA largely overestimated the localised strain amplitude as expected [10, 11]. The FEA modelled ideal fibre configurations for two fibre halves to predict strain patterns based on the local fibre orientation. It did not replicate the geometry of the ROIs or their surrounding strain fields. The quantitative comparison included thus more discrepancies than only due to the material properties. Some comments on the strain values in the quantitative comparison are included in appendix F.2.

4.6 Recommendations for nanoscale Digital Image Correlation methodology

The previous sections have demonstrated that nano-DIC allows identifying regions of strain concentration and have shown interesting results on the failure strains and submicron shear bands. There appears to be still room for further research with nano-DIC on composites and the following sections will elaborate on a quantitative comparison of composites, the restriction due to out-of-plane deformation and the magnification range.

4.6.1 Suggestions for quantitative comparison of composites

Two composites were subjected to nano-DIC, glass-PMMA and carbon-epoxy (section 3.1). Until now, no comparison of the strain localisation has been made between those composites. All the strain localisation patterns from the previous results were observed in both composites. As expected for glassy polymers (section 2.2.1), both matrices behave qualitatively in a similar way. For a quantitative comparison, not enough data was acquired during this master's thesis. The following suggestion is made to obtain comparable data sets for the two composites.

To characterise the local properties of the two matrices, similar geometries should be compared. This consists of equal fibre orientations as described in section 3.4 and even better similar fibre configurations of the surrounding fibres. A comparable in-situ matrix effect can be assessed by matching similar M/F geometries. In this manner, the effect of larger GFs could be accounted for ($\varnothing = \pm 15$ µm for glass vs. ± 7 µm for CFs). Thought should also be brought to the local strain intensity values. Both composites have different failure strains and one could think of normalising the local strains with the macroscopic stress-strain curves from previous research.

4.6.2 Restriction due to out-of-plane deformation

Severe out-of-plane deformations have been observed for horizontal configurations during the in-situ compression and have been confirmed by FEA as can be seen in Figure 4.20. DIC is a two-dimensional method, not able to measure out-of-plane displacements and will give falsified values in such cases. One should avoid these horizontal configurations in its analysis or could use stereo DIC to overcome this problem. More out-of-plane FEA strain maps are included in appendix F.3.

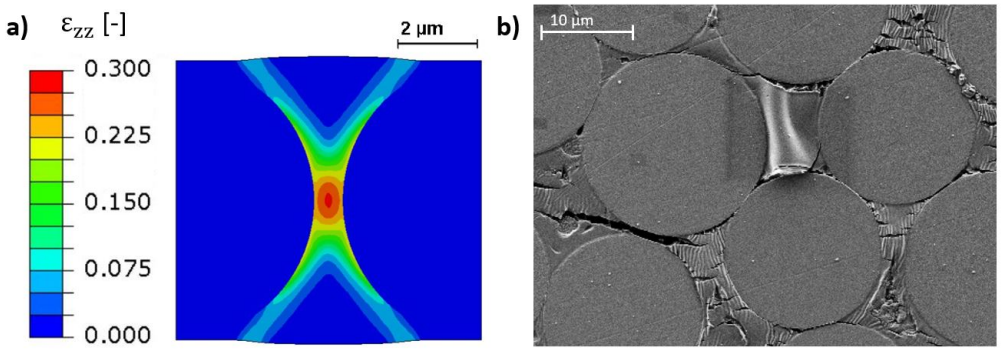

FIGURE 4.20: Out-of-plane deformation: (a) out-of-plane strain map from FEA for $M/F = 0.143$ and $U_x = -0.35$ µm and (b) post-mortem SEM micrograph of a horizontal glass-PMMA composite with $M/F = 0.24$.

4.6.3 Magnification range

The speckle pattern described in section 3.2 allowed for a magnification range from 5 000 x to 20 000 x with the best results at 10 000 x. The high magnification of 20 000 x could only be analysed with VIC-2D as this software includes smaller subset sizes, whereas Ncorr could only analyse up to 15 000 x (Figure 4.21).

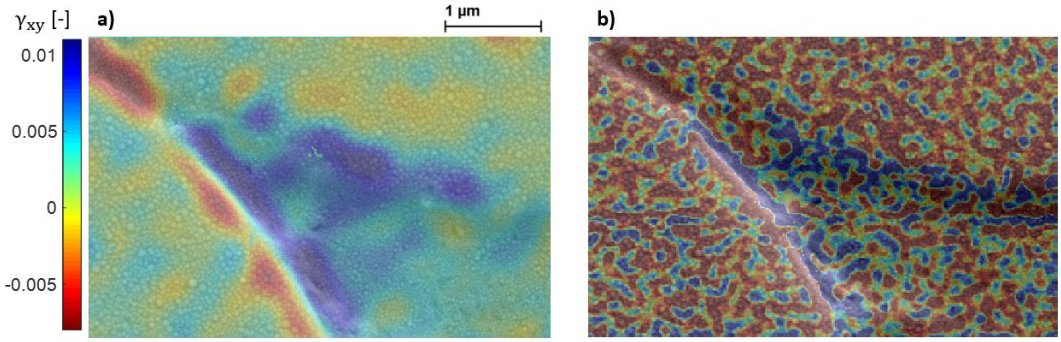

FIGURE 4.21: Shear strain maps at a magnification of 20 000 x by two DIC software packages: (a) VIC-2D and (b) Ncorr. The ROI includes a diagonal fibre configuration of a glass-PMMA composite with $M/F = 0.02$ and $\varepsilon_{xx,macro} = -0.101$

The magnification could be adapted in further work to capture ROIs of different sizes. This study used nano-DIC to focus on ROIs with two fibres and previous research has been conducted with µDIC on ROIs with approximately 20 fibres [11,50]. A mesoscale DIC could be interesting to capture 4-10 fibres. The speckle size should always correspond with the magnification and this can be tuned with the deposition time (Figure 2.7) [10]. For a higher scale, larger speckles are needed and thus a longer deposition time is required. For a fixed magnification and speckle size, one should also check the subset sizes of the DIC software to reduce noise on the strain fields.

Chapter 5

Conclusion and future work

This master's thesis was situated in the current search of the scientific community to provide physics-based microscale models to feed the multiscale models of composite structures. Its aim was to use nano-DIC on FRPs to study the behaviour of the matrix confined in between the fibres. Three fibre configurations, i.e. horizontal, vertical, and diagonal, were analysed for two composites, i.e. glass-PMMA and carbon-epoxy. The carbon-epoxy results were compared to FE predictions, which qualitatively yielded similar patterns. This master's thesis (1) consolidated the use of nano-DIC for the characterisation of FRPs at the fibre/matrix level, (2) provided a systematic semi-quantitative framework to analyse and compare nano-DIC results across different systems, and (3) created valuable data for experimental validation of micromechanical models. The more detailed conclusions are as follows:

- Based on a software comparison and a strain deviation analysis, Ncorr has been opted for as the optimal DIC software for this study. Both software packages (Ncorr and VIC-2D) could correctly compute average strains and were able to reveal strain localisation.
- Nano-DIC could successfully capture strain localisation at the fibre/matrix level. A clear distinction was observed between the fibre and the matrix response, with the matrix carrying the transverse compressive deformation. A distinct strain gradient was detected at the fibre/matrix interface, overcoming the smoothening of the µDIC technique.
- Compressive strain concentrations along the direction of compression were systematically observed along the perpendicular fibre interface in the ε_{xx}-maps. This strain pattern was confirmed for both composites, the three fibre configurations and by the FEA.
- No obvious strain localisation was captured by nano-DIC in the ε_{yy}-maps, whereas FEA predicted a large hourglass-shaped localised strain area in the matrix strip in between the fibres.

- Submicron shear bands were detected by nano-DIC in the γ_{xy}-maps. This strain pattern was confirmed for both composites, the three fibre configurations and by the FEA. The shear bands did not propagate through the matrix strip in between the fibres and remained localised at the fibre/matrix interface. Two trends were distinguished for the shear band evolution with increasing strain. Shear bands with their base oriented along the transverse tensile strain, e.g. horizontal fibre configurations, grew by increasing strain amplitude and broadening along the fibre/matrix interface. Shear bands with their base oriented perpendicular to the transverse tensile strain, e.g. vertical fibre configurations, intensified in strain amplitude at a fixed position. A combination of both cases was observed in diagonal configurations. The shear band orientation in vertical fibre configurations increased with the matrix strip length in between the fibres and the nano-DIC values coincided well with the literature. The FEA shear band orientation was systematically lower and pointed towards a difference between the in-situ matrix properties and the bulk properties used in the FEA.

- The failure locations in the ROI could be pre-emptively identified via strain concentrations in the γ_{max}-maps. The nano-strains at local failure were comparable to the corresponding macro-strains at local failure and lower than the macro-strains at macroscopic failure. This suggested a local increase in stress triaxiality, e.g. biaxial tension due to splitting of the fibre/matrix interface.

- Qualitatively, the FEA showed the same strain localisation patterns as nano-DIC, proving the importance of the fibre configuration on strain localisation phenomena. Quantitatively, the FEA overestimated the strain amplitudes and these discrepancies gave insight into the restrictions of existing computational models for FRPs. This study was not able to identify improvements for modelling but suggested further investigation of missing in-situ matrix effects and the interphase as input values.

The suggestions for future work include some extensions and alternative approaches for the experimental work, the data analysis and the FEA. For the experimental work, more nano-DIC tests would be interesting, to be able to statistically confirm the results mentioned above. More nano-DIC tests with comparable M/F geometries could also allow a quantitative comparison of composites. The ROIs for nano-DIC tests should be chosen with care, i.e. avoid out-of-plane deformation and stay within the measurable magnification range. Additionally, images on a much larger scale can be taken for each local image. Performing DIC on the larger ROIs with the fibres as speckle pattern, could provide a way to obtain macroscopic strains. These macroscopic strains could then be used in the comparison of local failure strains and bulk strains. Mesoscale DIC could give an interesting insight into the behaviour of groups of 4-10 fibres. It would bridge the gap between nano-DIC and µDIC by studying the effect of the local fibre configuration on strain localisation. The speckle size would need to be adapted for

meso-DIC by tuning the speckle deposition time. Stereo-DIC could be used at the nanoscale to assess out-of-plane deformations and the effect of differential erosion during polishing on the current data.

The nano-DIC data obtained during this work could be further analysed. Klavzer et al. [10] have shown that nano-DIC also allows investigating the interphase behaviour. The data from this study can serve to feed FEA with a strain gradient plasticity or include an interphase region around the fibres. The software comparison could be enhanced by comparing equal subset areas. More freedom in the DIC parameter choice can be obtained by reducing the correlation threshold.

More extensive modelling would be a final refined addition. The FEA from this study could be repeated for the glass-PMMA composite. The FEAs with two fibre halves could have additional matrix strips next to the fibres to avoid edge effects. The ROIs could also be entirely reconstructed in FEAs, as was done by Klavzer et al. [10], to assess the overestimation of the strain concentrations. This would consist of recreating the exact fibre configurations and applying the nano-DIC displacements as boundary conditions.

Appendices

Appendix A

Complements of materials and methods

A.1 Graphical representation of experimental procedure

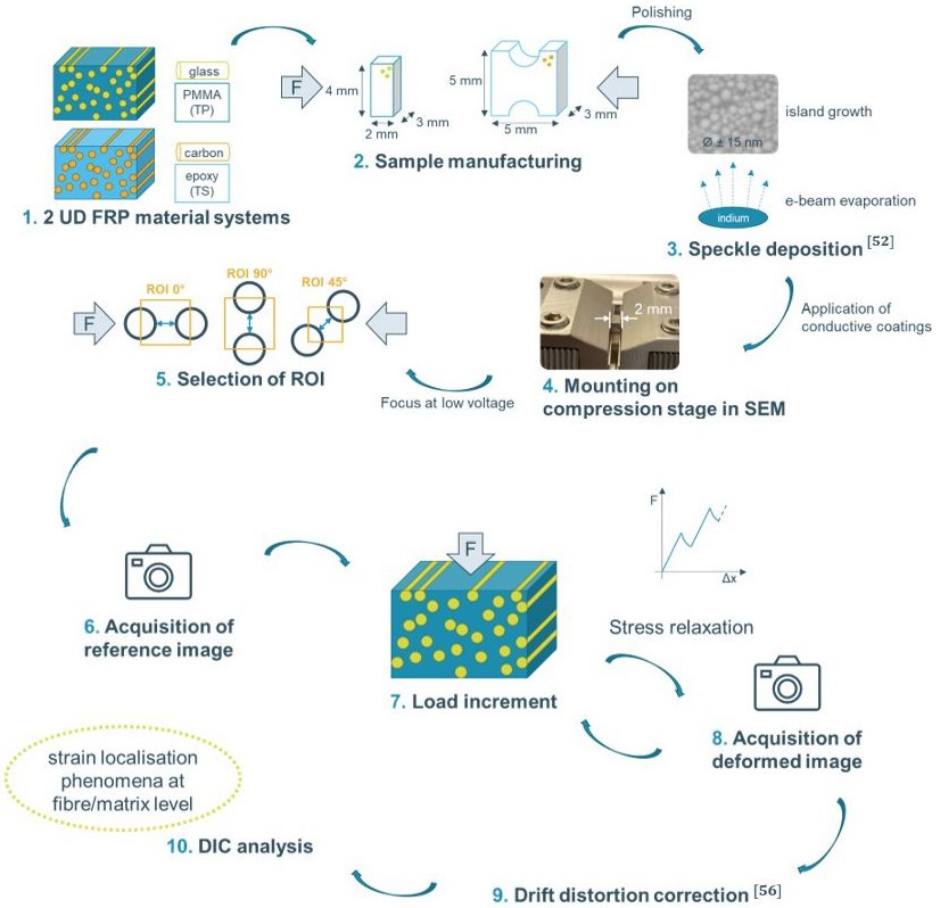

A.2 Load-displacement curve of compressed samples

Three glass-PMMA composite samples and three carbon-epoxy ones were transversely compressed. The load-displacement curves were obtained from the load cell and a stress-strain curve was computed for each sample from equations 3.6 and 3.8.

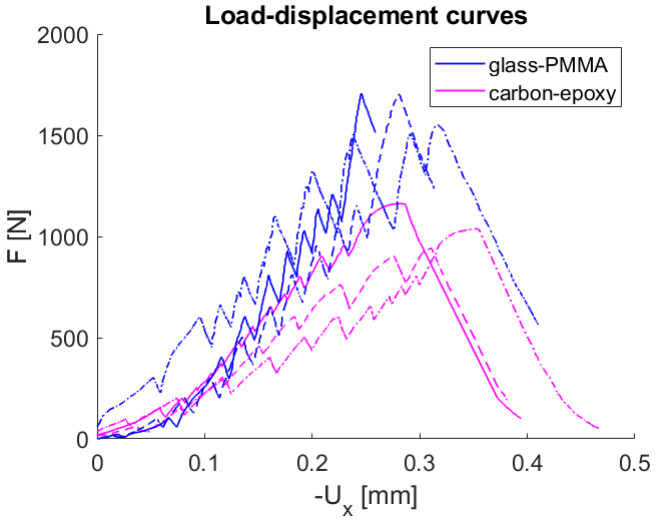

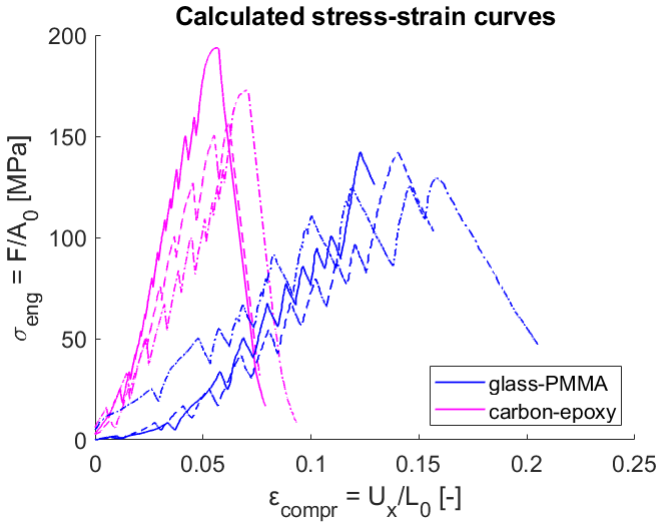

A.3 Drucker-Prager model for RTM6

The Drucker-Prager model for RTM6 developed by Morelle et al. [62] was implemented in the FEA to simulate rate-dependent elastoplastic epoxy.

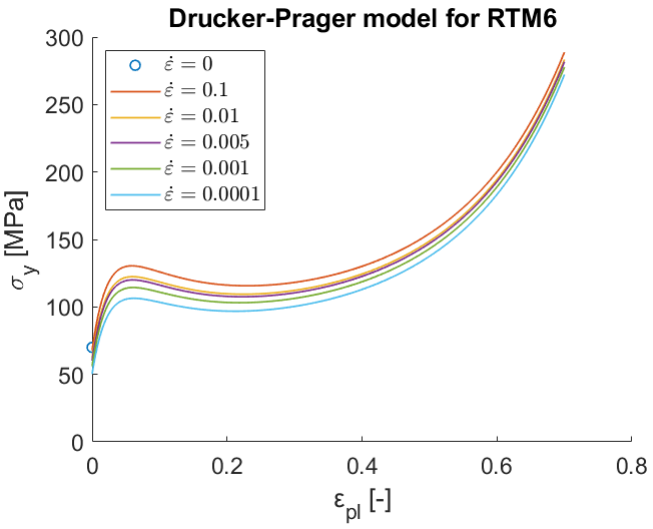

Appendix B

DIC software packages comparison results

B.1 Nano-DIC strain maps from software interface

The strain fields were mapped with two different software packages, Ncorr and VIC-2D. The maps displayed on each software interface revealed the effect of colour scaling on the interpretation of nano-DIC results.

B.1.1 Nano-DIC γ_{xy}^{log}-map of carbon-epoxy by Ncorr

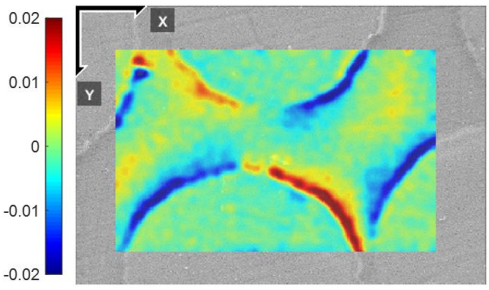

B.1.2 Nano-DIC γ_{xy}^{log}-map of carbon-epoxy by VIC-2D

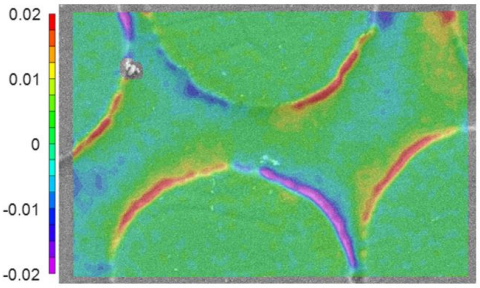

B.2 Nano-DIC strain map comparison

The nano-DIC results of the two software packages were compared for a carbon-epoxy composite and a glass-PMMA composite. The mean strain and the standard deviation of each strain map were computed and displayed. The mean strain and standard deviation of VIC-2D were on average lower than those of Ncorr.

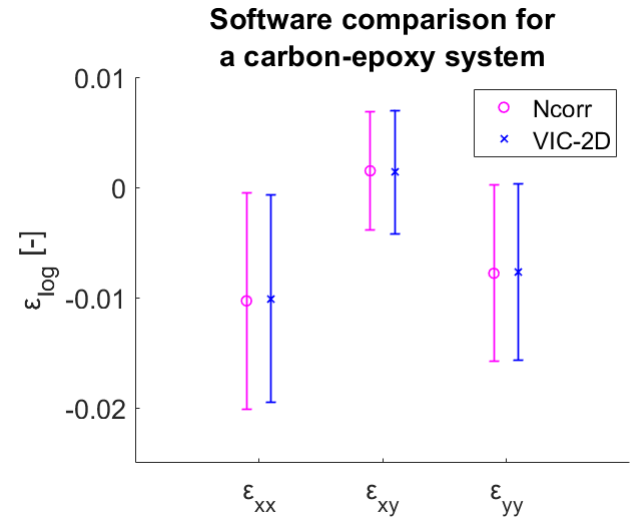

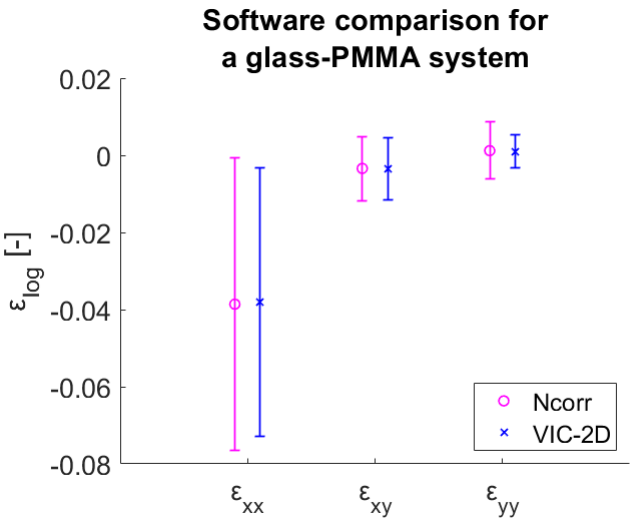

Appendix C

Strain localisation results

C.1 Transverse strain maps in x-direction

Compressive strain concentrations along the direction of compression were systematically observed along the perpendicular fibre interface in all three fibre configurations. This trend was captured by nano-DIC in both the carbon-epoxy and glass-PMMA composites and simulated in the FEAs.

C.1.1 Nano-DIC ε_{xx}^{log}-maps for three fibre configurations

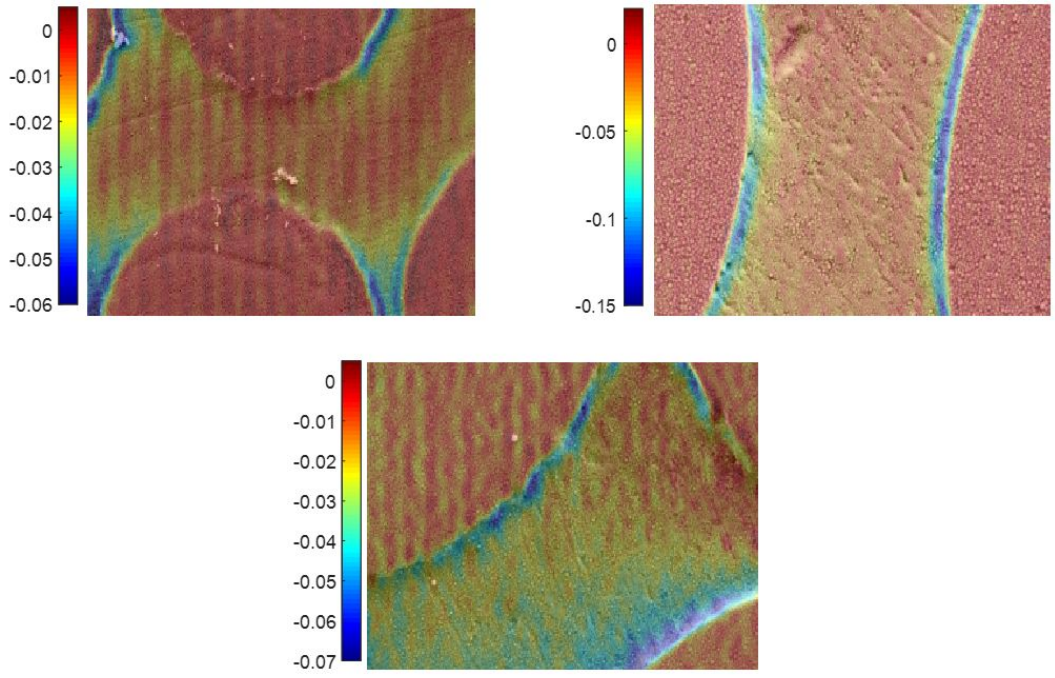

C.1.2 FEA ε_{xx}^{log}-maps for RTM6 with M/F = 0.286 at U_x = -0.35µm

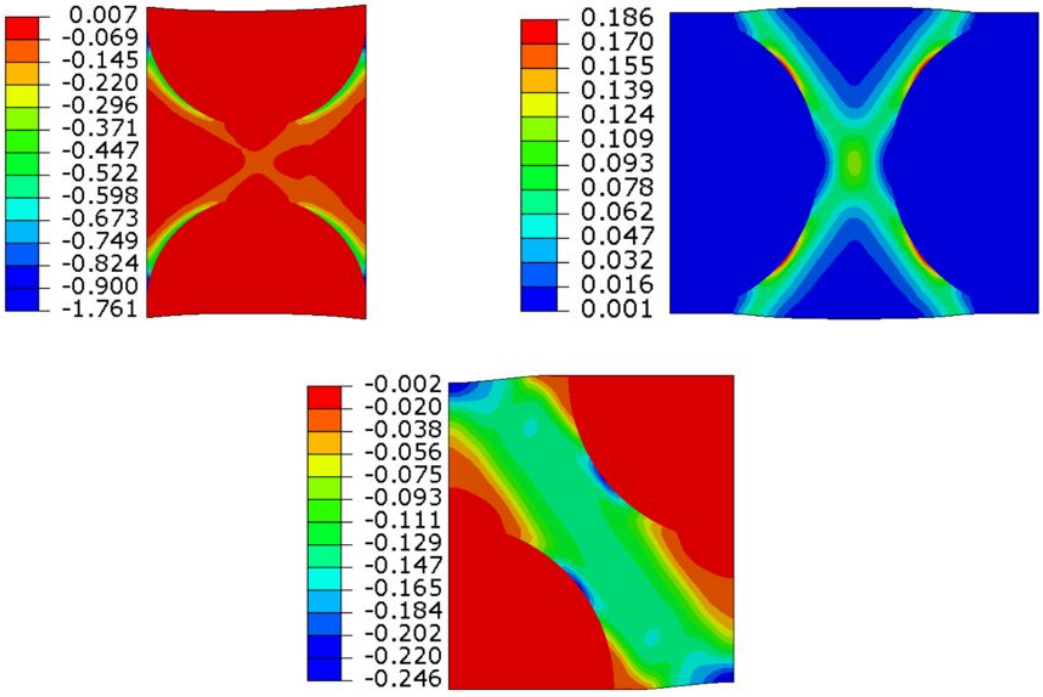

C.2 Principal strains

The principal strains ε_1 and ε_2 corresponded respectively with the experimental normal strains ε_{yy} and ε_{xx}.

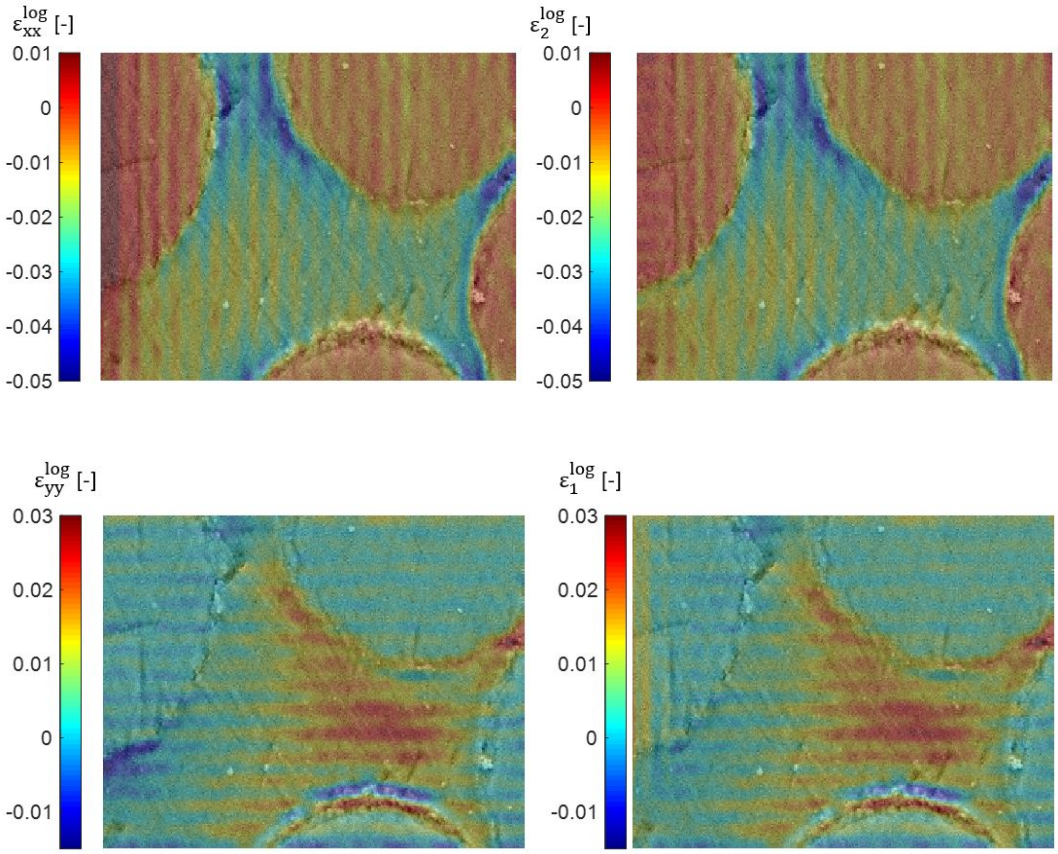

Appendix D

Failure results

D.1 Prediction of failure location in nano-DIC maximal shear strain maps

Maximal shear strain localisations were seen to coincide with the failure locations for the three fibre configurations in both material systems.

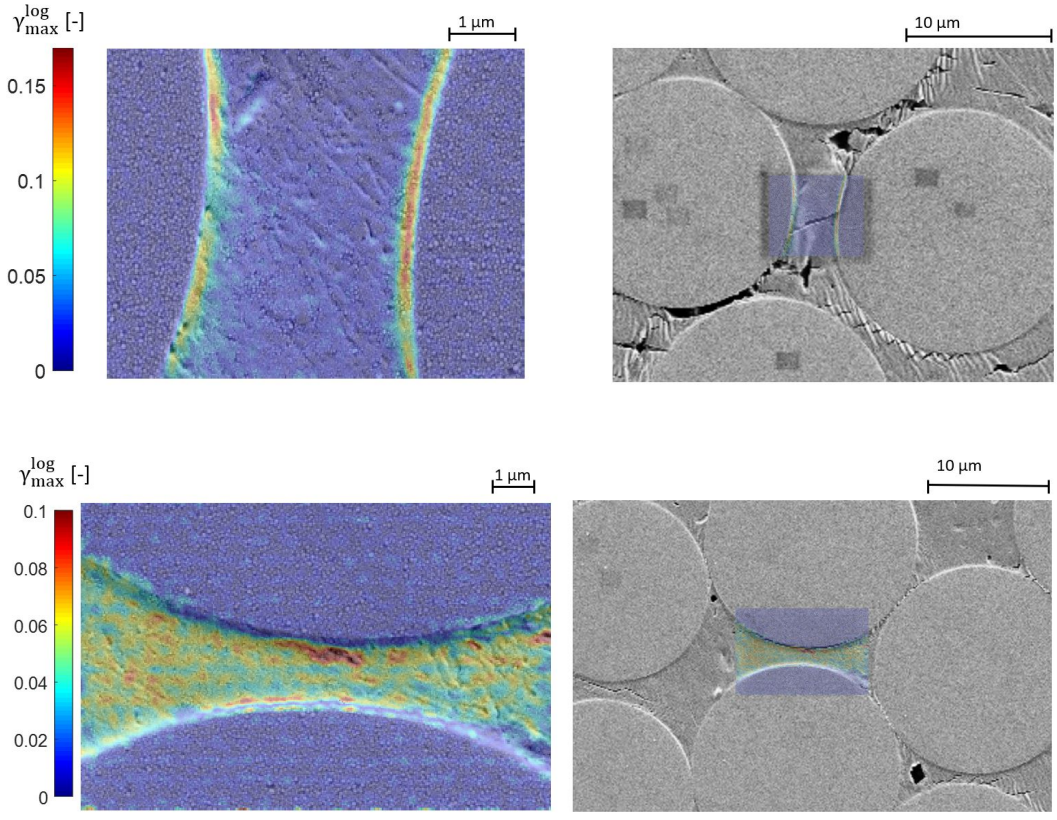

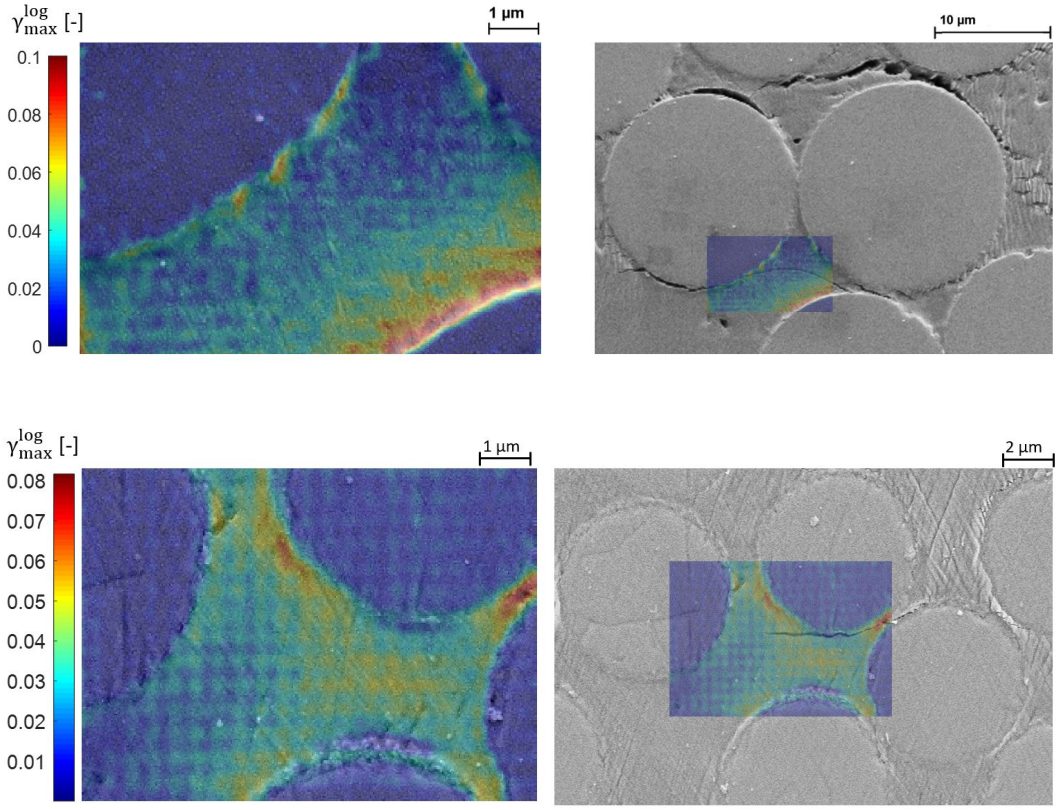
γ_{max}^{log} [-]
0.1
0.08
0.06
0.04
0.02
0
1 µm
10 µm
γ_{max}^{log} [-]
0.08
0.07
0.06
0.05
0.04
0.03
0.02
0.01
1 µm
2 µm

D.2 Post-mortem SEM micrographs of the failed material surface

Fracture surface micrographs on several lengths scales confirmed that the glass-PMMA composite displays ductile behaviour and the carbon-epoxy composite behaves in a brittle manner.

D.2.1 Glass fibre-reinforced Elium

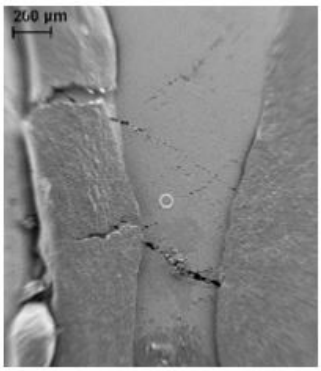

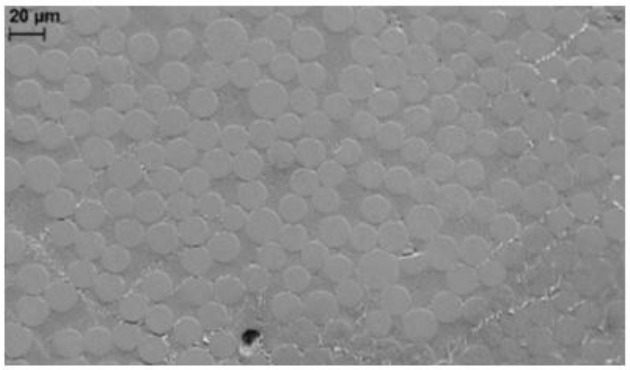

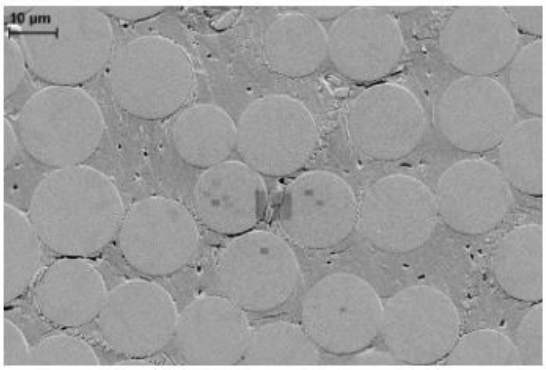

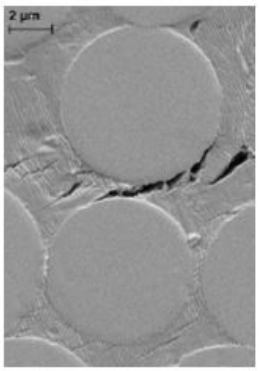

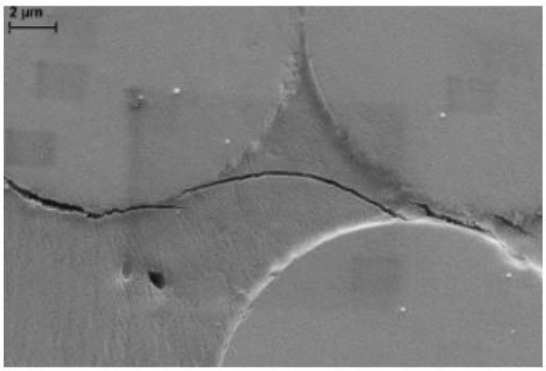

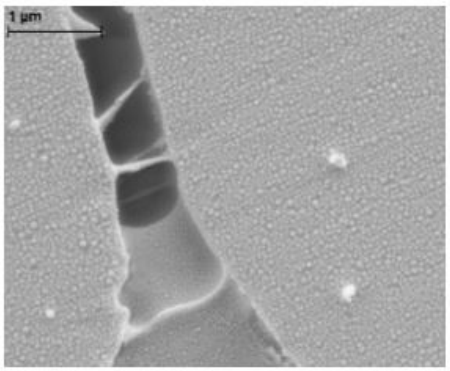

D.2.2 Carbon fibre-reinforced RTM6

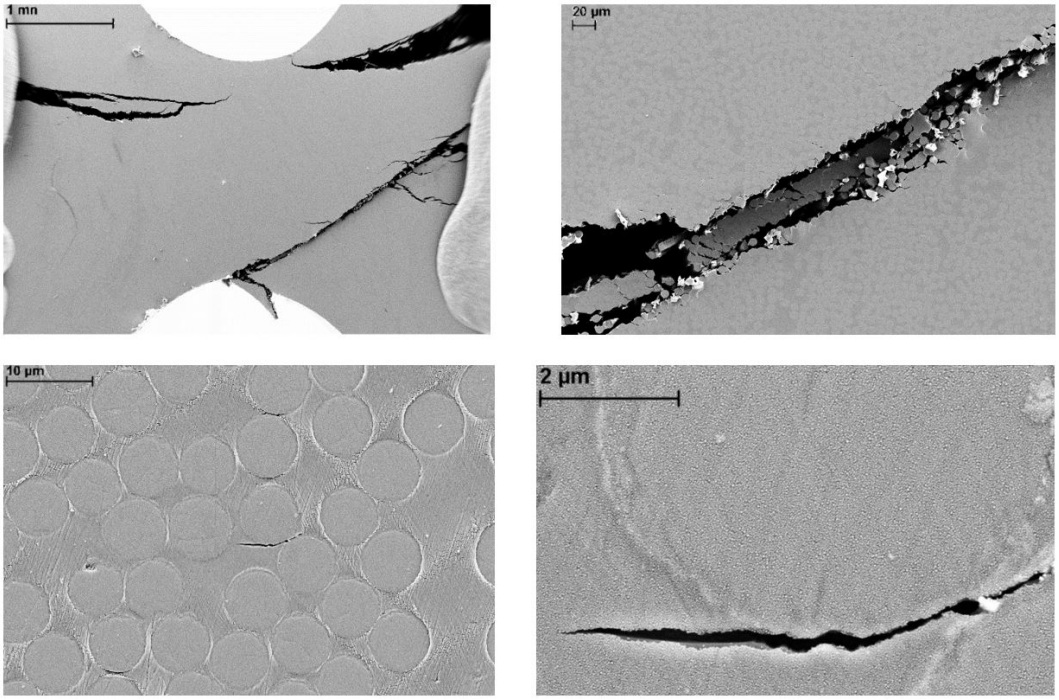

Appendix E

Submicron shear bands results

E.1 Shear band dimensions

Shear bands were recognised in the X-shaped patterns of both nano-DIC and FEA. The following dimension methodology was proposed. The ends of the shear strain localisation zones were connected and the angles were measured with ImageJ (National Institutes of Health, Maryland, USA) as indicated. The shear band angle was obtained as the average of the upper and lower angle. The shear band base was obtained by:

$$\text{shear band base} = (\text{matrix strip length}) * \tan\left(\frac{\text{shear band angle}}{2}\right) \tag{E.1}$$

and the shear band orientation by

$$\text{shear band orientation} = 90° - \frac{\text{shear band angle}}{2} \tag{E.2}$$

respective to the loading direction.

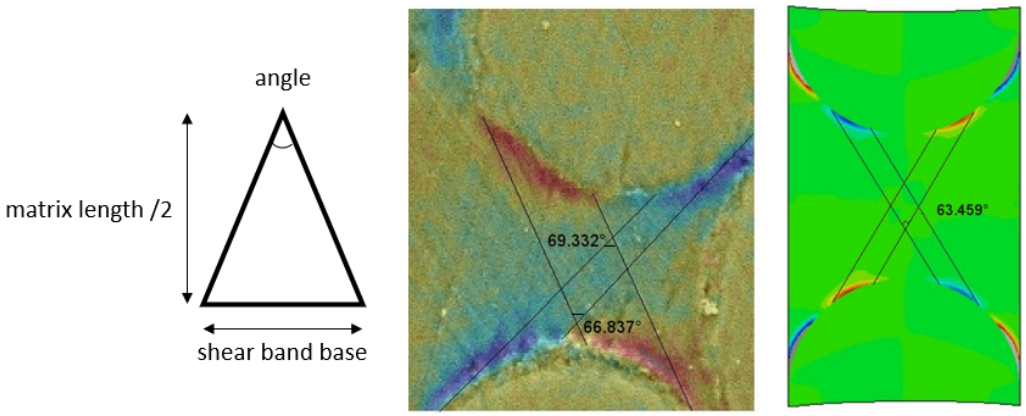

E.2 FEA shear band evolution with increasing strain

Shear strain maps were obtained by FEAs for the carbon-epoxy composite at $U_x = -0.35$ µm in three fibre configurations with increasing M/F.

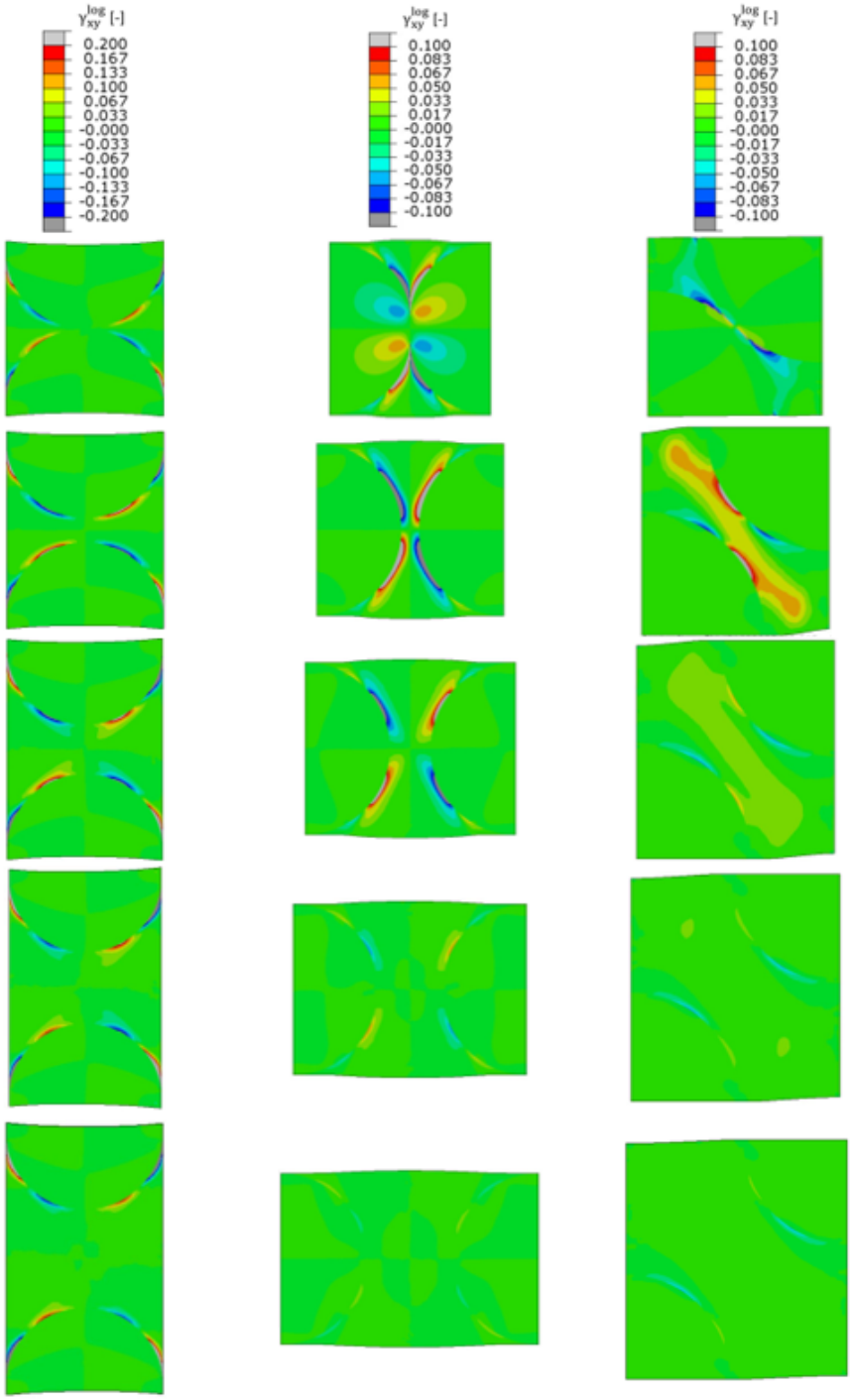

E.3 Drucker-Prager model for RTM6 increased by 20 %

The Drucker-Prager model for RTM6 as developed by Morelle et al. [62] was adapted by increasing the strength by 20 % over the whole strain softening and hardening regime.

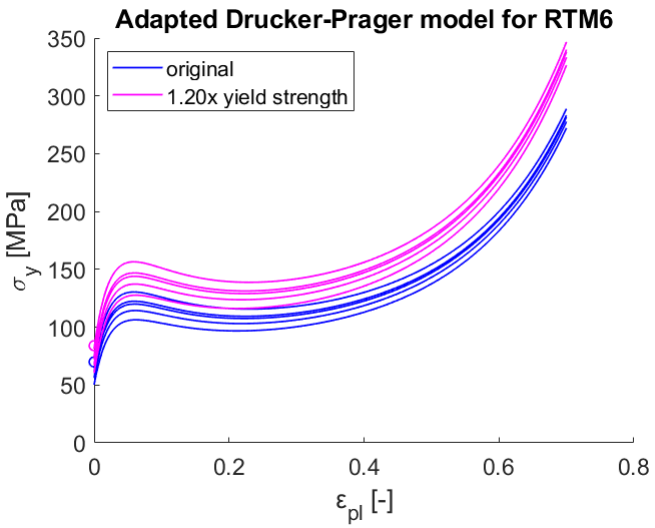

Appendix F

Comparison of Digital Image Correlation and Finite Element Analysis

F.1 Qualitative comparison

The strain localisation patterns observed in nano-DIC were compared to those of the FEA for a vertical carbon-epoxy configuration at $\varepsilon_{xx,micro} = -0.013$. Each FEA map, for a model with $M/F = 0.29$, and nano-DIC map, for an ROI with $M/F = 0.34$ and $\varepsilon_{xx,macro} = -0.055$, were studied at equal strain scales.

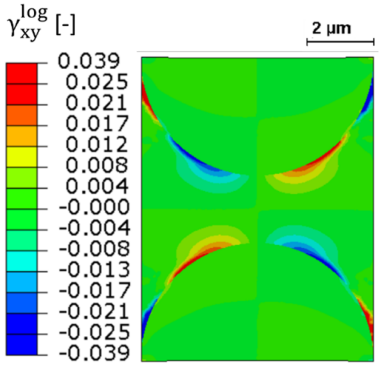

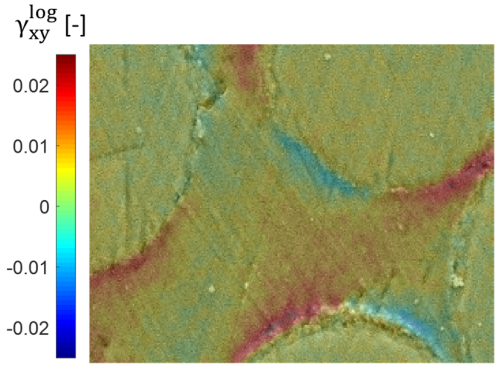

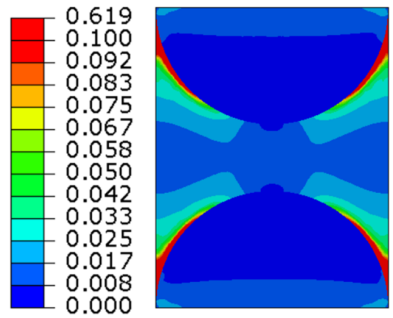

γ_{max}

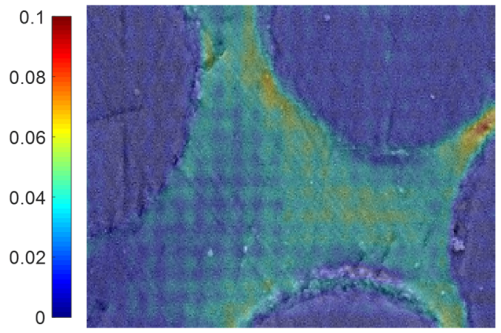

Mean $\gamma_{max} = 0.0213$

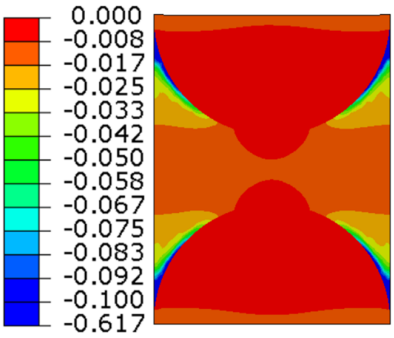

Mean $\varepsilon_{xx} = -0.0123$

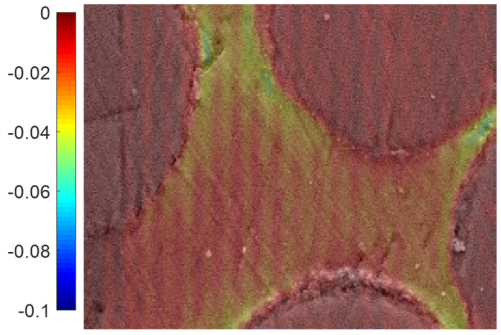

Mean $\varepsilon_{xx} = -0.0126$

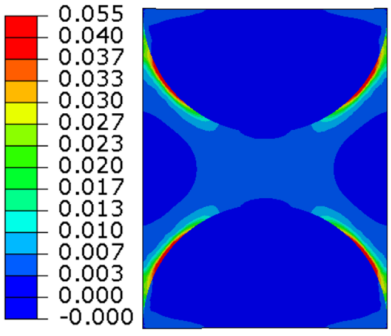

Mean $\varepsilon_{yy} = 0.0036$

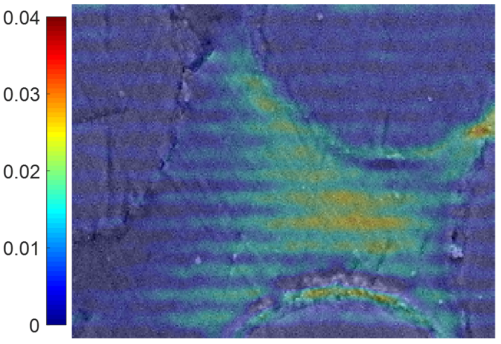

Mean $\varepsilon_{yy} = 0.0066$

F.2 Quantitative comparison

Quantitatively, the FEA largely diverged from the experimental nano-DIC values. The ε_{xx}, ε_{yy} and γ_{xy}-fields of two carbon-epoxy ROIs were compared with their corresponding simulation. On average for all those strain fields, the FEA yielded a mean strain that was in absolute value 58.3 % below those obtained by nano-DIC. The strain range from FEA was 267.0 % larger than for the nano-DIC-maps. This large contrast is partly related to the small mesh elements and boundary conditions mentioned in section 4.5 and to the inability of DIC to capture out-of-plane displacement, which was detailed in section 4.6.2. Since the variation between FEA and nano-DIC is that high, it could give insight into the restrictions of existing computational models for composite structures. The FEA included a Drucker-Prager criterion for the model validated at the macroscale and assumed perfect fibre/matrix interfaces but the nano-DIC values suggest otherwise. Note that the exact fibre configuration of the ROI was approximated in the FEA by two halve fibres, which is also contributing to the quantitative difference between FEA and nano-DIC. In further research, the exact geometries could be recreated and the applied boundary conditions on the edges of the respective ROIs determined from the displacement profiles measured by nano-DIC, as was done by Klavzer et al. [10].

F.3 Out-of-plane deformation

The FEA ε_{zz}^{log}-maps for RTM6 with $M/F = 0.286$ at U_x = -0.35 µm predicted out-of-plane deformations in the three fibre configurations.

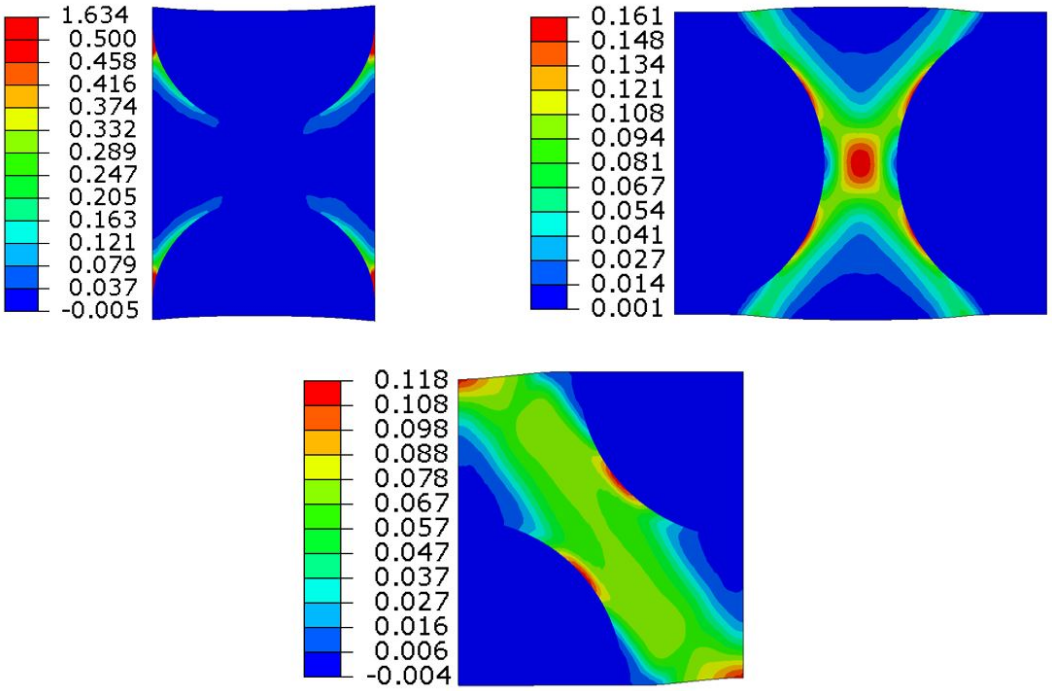

Bibliography

[1] J. Qureshi. A review of fibre reinforced polymer structures. *Fibers*, 10(3), 2022.

[2] H. Helms and U. Lambrecht. The potential contribution of light-weighting to reduce transport energy consumption. *Int. J. Life Cycle Assess*, 12(1):58–64, 2007.

[3] J. Hale. Boeing 787, from the ground up, 2006. Accessed May 22, 2023. `https://www.boeing.com/commercial/aeromagazine/articles/qtr_4_06/article_04_2.html`.

[4] Airbus. Airbus commends global agreement on co2 standard, 2016. Accessed May 22, 2023. `https://www.airbus.com/en/newsroom/press-releases/2016-02-airbus-commends-global-agreement-on-co2-standard`.

[5] J. Chevalier. *Micromechanics of an epoxy matrix for fiber reinforced composites: experiments and physics-based modelling*. PhD thesis, UCL-Université Catholique de Louvain, 2018.

[6] B. Cox and Q. Yang. In quest of virtual tests for structural composites. *Science*, 314(5802):1102–1107, 2006.

[7] J. LLorca, C. González, J.M. Molina-Aldareguía, J. Segurado, R. Seltzer, F. Sket, M. Rodríguez, S. Sádaba, R. Muñoz, and L.P. Canal. Multiscale modeling of composite materials: a roadmap towards virtual testing. *Advanced materials*, 23(44):5130–5147, 2011.

[8] J. LLorca, C. González, J.M. Molina-Aldareguía, and C.S. Lopes. Multiscale modeling of composites: toward virtual testing... and beyond. *Jom*, 65:215–225, 2013.

[9] T. Pardoen, N. Klavzer, S. Gayot, F. Van Loock, J. Chevalier, X. Morelle, V. Destoop, F. Lani, P. Camanho, L. Brassart, et al. Nanomechanics serving polymer-based composite research. *Comptes Rendus. Physique*, 22(S3):331–352, 2021.

[10] N. Klavzer, S.F. Gayot, M. Coulombier, B. Nysten, and T. Pardoen. Nanoscale digital image correlation at elementary fibre/matrix level in polymer-based composites. *Composites Part A: Applied Science and Manufacturing*, 168:107455, 2023.

[11] J. Chevalier, P.P. Camanho, F. Lani, and T. Pardoen. Multi-scale characterization and modelling of the transverse compression response of unidirectional carbon fiber reinforced epoxy. *Composite Structures*, 209:160–176, 2019.

[12] J.R. Gregory and S.M. Spearing. Nanoindentation of neat and in situ polymers in polymer-matrix composites. *Composites Science and Technology*, 65(3):595–607, 2005.

[13] M. Hardiman, T.J. Vaughan, and C.T. McCarthy. Fibrous composite matrix characterisation using nanoindentation: The effect of fibre constraint and the evolution from bulk to in-situ matrix properties. *Composites Part A: Applied Science and Manufacturing*, 68:296–303, 2015.

[14] T. Hobbiebrunken, B. Fiedler, M. Hojo, and M. Tanaka. Experimental determination of the true epoxy resin strength using micro-scaled specimens. *Composites Part A: Applied Science and Manufacturing*, 38(3):814–818, 2007.

[15] J. Misumi, R. Ganesh, S. Sockalingam, and J.W. Gillespie Jr. Experimental characterization of tensile properties of epoxy resin by using micro-fiber specimens. *Journal of Reinforced Plastics and Composites*, 35(24):1792–1801, 2016.

[16] X. Sui, M. Tiwari, I. Greenfeld, R.L. Khalfin, H. Meeuw, B. Fiedler, and H.D. Wagner. Extreme scale-dependent tensile properties of epoxy fibers. *eXPRESS polymer letters*, 13(11):993–1003, 2019.

[17] O. Verschatse, L. Daelemans, W. Van Paepegem, and K. De Clerck. In-situ observations of microscale ductility in a quasi-brittle bulk scale epoxy. *Polymers*, 12(11), 2020.

[18] T.D. Downing, R. Kumar, W.M. Cross, L. Kjerengtroen, and J.J. Kellar. Determining the interphase thickness and properties in polymer matrix composites using phase imaging atomic force microscopy and nanoindentation. *Journal of adhesion science and technology*, 14(14):1801–1812, 2000.

[19] V. Cech, E. Palesch, and J. Lukes. The glass fiber-polymer matrix interface/interphase characterized by nanoscale imaging techniques. *Composites Science and Technology*, 83:22–26, 2013.

[20] S. Waghmare, S. Shelare, K.nAglawe, and P. Khope. A mini review on fibre reinforced polymer composites. *Materials Today: Proceedings*, 54:682–689, 2022.

[21] I.S. Abbood, S.A. Odaa, K.F. Hasan, and M.A. Jasim. Properties evaluation of fiber reinforced polymers and their constituent materials used in structures - a review. *Materials Today: Proceedings*, 43:1003–1008, 2021.

[22] Y. Hu, N.K. Kar, and S.R. Nutt. Transverse compression failure of unidirectional composites. *Polymer Composites*, 36(4):756–766, 2015.

[23] L. Yang, Y. Yan, Y. Liu, and Z. Ran. Microscopic failure mechanisms of fiber-reinforced polymer composites under transverse tension and compression. *Composites Science and Technology*, 72(15):1818–1825, 2012.

[24] E. Totry, J.M. Molina-Aldareguía, C. González, and J. LLorca. Effect of fiber, matrix and interface properties on the in-plane shear deformation of carbon-fiber reinforced composites. *Composites Science and Technology*, 70(6):970–980, 2010.

[25] A. Jonas. *LMAPR2019A - Polymer Science and Engineering A: Physics*. UCLouvain, 2020.

[26] X. Morelle. *Mechanical characterization and physics-based modeling of highly-crosslinked epoxy resin*. PhD thesis, UCL-Université Catholique de Louvain, 2015.

[27] H.E.H. Meijer and L.E. Govaert. Mechanical performance of polymer systems: The relation between structure and properties. *Progress in Polymer Science*, 30(8):915–938, 2005. Plenary Lectures.

[28] M.F. Ashby. *Materials Selection in Mechanical Design*. Butterworth-Heinemann, Oxford, fourth edition edition, 2011.

[29] W. Obande, D. Mamalis, D. Ray, L. Yang, and C.M. Ó Brádaigh. Mechanical and thermomechanical characterisation of vacuum-infused thermoplastic- and thermoset-based composites. *Materials & Design*, 175:107828, 2019.

[30] W. Obande, C.M. Ó Brádaigh, and D. Ray. Continuous fibre-reinforced thermoplastic acrylic-matrix composites prepared by liquid resin infusion - a review. *Composites Part B: Engineering*, 215:108771, 2021.

[31] C. G'sell and J.J. Jonas. Yield and transient effects during the plastic deformation of solid polymers. *Journal of Materials Science*, 16:1956–1974, 1981.

[32] A.S. Argon and M.I. Bessonov. Plastic flow in glassy polymers. *Polymer Engineering & Science*, 17(3):174–182, 1977.

[33] L.C.A. van Breemen, E.T.J. Klompen, L.E. Govaert, and H.E.H. Meijer. Extending the egp constitutive model for polymer glasses to multiple relaxation times. *Journal of the Mechanics and Physics of Solids*, 59(10):2191–2207, 2011.

[34] S. Rabinowitz, I.M. Ward, and J.S.C. Parry. The effect of hydrostatic pressure on the shear yield behaviour of polymers. *Journal of Materials science*, 5:29–39, 1970.

[35] P.B. Bowden. *The Yield Behaviour of Glassy Polymers*, pages 279–339. Springer Netherlands, Dordrecht, 1973.

[36] C. G'sell and J.J. Jonas. Determination of the plastic behaviour of solid polymers at constant true strain rate. *Journal of materials science*, 14(3):583–591, 1979.

[37] O.A. Hasan and M.C. Boyce. A constitutive model for the nonlinear viscoelastic viscoplastic behavior of glassy polymers. *Polymer Engineering & Science*, 35(4):331–344, 1995.

[38] O. Sindt, J. Perez, and J.F. Gerard. Molecular architecture-mechanical behaviour relationships in epoxy networks. *Polymer*, 37(14):2989–2997, 1996.

[39] C. G'sell and A.J. Gopez. Plastic banding in glassy polycarbonate under plane simple shear. *Journal of Materials Science*, 20:3462–3478, 1985.

[40] D.J.A. Senden, J.A.W. Van Dommelen, and L.E. Govaert. Strain hardening and its relation to bauschinger effects in oriented polymers. *Journal of Polymer Science Part B: Polymer Physics*, 48(13):1483–1494, 2010.

[41] R.S. Hoy and M.O. Robbins. Strain hardening of polymer glasses: Effect of entanglement density, temperature, and rate. *Journal of Polymer Science Part B: Polymer Physics*, 44(24):3487–3500, 2006.

[42] H.G.H. van Melick, L.E. Govaert, and H.E.H. Meijer. On the origin of strain hardening in glassy polymers. *Polymer*, 44(8):2493–2502, 2003.

[43] L.P. Canal, C. González, J.M. Molina-Aldareguía, J. Segurado, and J. LLorca. Application of digital image correlation at the microscale in fiber-reinforced composites. *Composites Part A: Applied Science and Manufacturing*, 43(10):1630–1638, 2012. CompTest 2011.

[44] M. Hardiman, T.J. Vaughan, and C.T. McCarthy. A review of key developments and pertinent issues in nanoindentation testing of fibre reinforced plastic microstructures. *Composite Structures*, 180:782–798, 2017.

[45] S. Subramanian, J.J. Lesko, K.L. Reifsnider, and W.W. Stinchcomb. Characterization of the fiber-matrix interphase and its influence on mechanical properties of unidirectional composites. *Journal of Composite Materials*, 30(3):309–332, 1996.

[46] C. González and J. LLorca. Mechanical behavior of unidirectional fiber-reinforced polymers under transverse compression: Microscopic mechanisms and modeling. *Composites Science and Technology*, 67(13):2795–2806, 2007.

[47] M. Bornert, F. Brémand, P. Doumalin, J-C. Dupré, M. Fazzini, M. Grédiac, F. Hild, S. Mistou, J. Molimard, J-J. Orteu, et al. Assessment of digital image correlation measurement errors: methodology and results. *Experimental mechanics*, 49:353–370, 2009.

[48] J. Blaber, B. Adair, and A. Antoniou. Ncorr: open-source 2d digital image correlation matlab software. *Experimental Mechanics*, 55(6):1105–1122, 2015.

[49] F. Lagattu, F. Bridier, P. Villechaise, and J. Brillaud. In-plane strain measurements on a microscopic scale by coupling digital image correlation and an in situ sem technique. *Materials Characterization*, 56(1):10–18, 2006.

[50] M. Mehdikhani, M. Aravand, B. Sabuncuoglu, M.G. Callens, S.V. Lomov, and L. Gorbatikh. Full-field strain measurements at the micro-scale in fiber-reinforced composites using digital image correlation. *Composite Structures*, 140:192–201, 2016.

[51] M. Mehdikhani, A. Matveeva, M.A. Aravand, B.L. Wardle, S.V. Lomov, and L. Gorbatikh. Strain mapping at the micro-scale in hierarchical polymer composites with aligned carbon nanotube grafted fibers. *Composites Science and Technology*, 137:24–34, 2016.

[52] J.P.M. Hoefnagels, M.P.F.H.L. van Maris, and T. Vermeij. One-step deposition of nano-to-micron-scalable, high-quality digital image correlation patterns for high-strain in-situ multi-microscopy testing. *Strain*, 55(6):e12330, 2019. e12330 STRAIN-1507.R1.

[53] J.L.W. Carter, Michael D. Uchic, and M.J. Mills. Impact of speckle pattern parameters on dic strain resolution calculated from in-situ sem experiments. In J. Carroll and S. Daly, editors, *Fracture, Fatigue, Failure, and Damage Evolution, Volume 5*, pages 119–126, Cham, 2015. Springer International Publishing.

[54] M.A. Sutton, N. Li, D.C. Joy, A.P. Reynolds, and X. Li. Scanning electron microscopy for quantitative small and large deformation measurements part i: Sem imaging at magnifications from 200 to 10,000. *Experimental mechanics*, 47:775–787, 2007.

[55] M.A. Sutton, N. Li, D. Garcia, N. Cornille, J-J. Orteu, S.R. McNeill, H.W. Schreier, X. Li, and A.P. Reynolds. Scanning electron microscopy for quantitative small and large deformation measurements part ii: experimental validation for magnifications from 200 to 10,000. *Experimental Mechanics*, 47:789–804, 2007.

[56] A.D. Kammers and S. Daly. Digital image correlation under scanning electron microscopy: methodology and validation. *Experimental Mechanics*, 53:1743–1761, 2013.

[57] W.C. Oliver and G.M. Pharr. An improved technique for determining hardness and elastic modulus using load and displacement sensing indentation experiments. *Journal of materials research*, 7(6):1564–1583, 1992.

[58] A. Bahrami, X. Morelle, L.D. Hông Minh, T. Pardoen, C. Bailly, and B. Nysten. Curing dependent spatial heterogeneity of mechanical response in epoxy resins revealed by atomic force microscopy. *Polymer*, 68:1–10, 2015.

[59] M. Greisel, J. Jäger, J. Moosburger-Will, M.G.R. Sause, W.M. Mueller, and S. Horn. Influence of residual thermal stress in carbon fiber-reinforced thermoplastic composites on interfacial fracture toughness evaluated by cyclic single-fiber push-out tests. *Composites Part A: Applied Science and Manufacturing*, 66:117–127, 2014.

[60] Correlated Solutions. Vic-2d reference manual, 2022. Accessed April 7, 2023. www.correlatedsolutions.com.

[61] Abaqus Inc. Abaqus/explicit, 2021. Accessed May 10, 2023. https://www.3ds.com/products-services/simulia/products/abaqus/abaqusexplicit/.

[62] X.P. Morelle, J. Chevalier, C. Bailly, T. Pardoen, and F. Lani. Mechanical characterization and modeling of the deformation and failure of the highly crosslinked rtm6 epoxy resin. *Mechanics of Time-Dependent Materials*, 21:419–454, 2017.

[63] P. Van Houtte and M. Seefeldt. *Mechanisch Gedrag van Materialen*. KU Leuven, 2017.

[64] S. Gayot, C. Bailly, T. Pardoen, J. Chevalier, and P. Gérard. Relationship between processing parameters and mechanical properties of thick glass fibre reinforced pmma composites. In *COMPOSITES 2019, 7th ECCOMAS Thematic Conference on the Mechanical Response of Composites*, 2019.

[65] J. Chevalier, X.P. Morelle, C. Bailly, P.P. Camanho, T. Pardoen, and F. Lani. Micro-mechanics based pressure dependent failure model for highly cross-linked epoxy resins. *Engineering Fracture Mechanics*, 158:1–12, 2016.

UNIVERSITÉ CATHOLIQUE DE LOUVAIN
École polytechnique de Louvain
Rue Archimède, 1 bte L6.11.01, 1348 Louvain-la-Neuve, Belgique | **www.uclouvain.be/epl**